POLITECNICO DI TORINO
Repository ISTITUZIONALE

Microstructural evolution and enhanced passivation mechanisms of metastable beta-titanium 21S in laser powder directed energy deposition

Original
Microstructural evolution and enhanced passivation mechanisms of metastable beta-titanium 21S in laser powder directed energy deposition / Sohrabi, A., Behjat, A., Mazzucato, F., Valente, A., Fattah-alhosseini, A., Chaharmahali, R., Iuliano, L., Saboori, A.. - In: JOURNAL OF ALLOYS AND COMPOUNDS. - ISSN 0925-8388. - 1084:(2026). [10.1016/j.jallcom.2026.191961]

Availability:
This version is available at: 11583/3017296 since: 2026-10-31T16:31:37Z

Publisher:
Elsevier

Published
DOI:10.1016/j.jallcom.2026.191961

Terms of use:

This article is made available under terms and conditions as specified in the corresponding bibliographic description in the repository

Publisher copyright

(Article begins on next page)

13 November 2026

Journal of Alloys and Compounds 1084 (2026) 191961

Contents lists available at ScienceDirect

Journal of Alloys and Compounds

journal homepage: www.elsevier.com/locate/jalcom

Microstructural evolution and enhanced passivation mechanisms of metastable beta-titanium 21S in laser powder directed energy deposition

Alireza Sohrabi [a], Amir Behjat [b,c,*], Federico Mazzucato [d], Anna Valente [d], Arash Fattah-alhosseini [e], Razieh Chaharmahali [f], Luca Iuliano [b,c], Abdollah Saboori [b,c,*]

[a] Department of Applied Science and Technology, Politecnico di Torino, Corso Duca degli Abruzzi 24, Torino, 1029, Italy
[b] Department of Management and Production Engineering, Politecnico di Torino, Corso Duca degli Abruzzi 24, Torino, 10129, Italy
[c] Integrated Additive Manufacturing Center (IAM@PoliTo), Politecnico di Torino, Corso Castelfidardo 51, Torino, 10129, Italy
[d] Department of Innovative Technologies, University of Applied Science and Arts of Southern Switzerland (SUPSI), Via La Santa 1, Lugano, 6962, Switzerland
[e] Department of Materials Engineering, Faculty of Engineering, Bu-Ali Sina University, Hamedan, Iran
[f] Department of Materials Engineering, Hamedan University of Technology, Hamedan, Iran

ARTICLE INFO

Keywords:
Beta-Titanium alloy
Ti-21S
Laser powder directed energy deposition
Additive manufacturing
Electrochemical
Ti alloys

ABSTRACT

Metastable beta-titanium alloys, such as Ti-21S (Ti–15Mo–3Nb–3Al–0.2Si wt%), offer an exceptional combination of high elevated-temperature strength, low elastic modulus, and outstanding corrosion resistance. However, their limited weldability and poor thermal conductivity present severe challenges for conventional manufacturing. While Laser Powder Directed Energy Deposition (LP-DED) provides a high-deposition-rate alternative, controlling the complex phase transformations under its rapid, cyclic thermal gradients remains highly erratic. Traditional parametric processing maps fail to account for this unique thermal history, leading to unpredictable multi-property trade-offs. To address this fundamental challenge, this study introduces a mechanistic approach that correlates the rapid solidification kinetics of LP-DED with the microstructural evolution and the defect structure of the resulting protective oxide films. By mapping the melt pool thermodynamics, near-fully dense (99.7–99.9%) components were successfully fabricated. The extreme thermal gradients suppressed alpha-phase precipitation, yielding a fully retained beta-microstructure that exhibited a characteristic low reduced elastic modulus (95–102 GPa) typical of metastable beta-titanium alloys alongside high microhardness (332–388 HV). Crucially, electrochemical evaluations reveal that the homogeneous solid-solution induced by LP-DED fundamentally alters the semiconducting properties of the passive film. The rapid solidification effectively traps high-valence Mo and Nb dopants, significantly reducing the concentration of oxygen vacancy donors and establishing robust resistance to aggressive environments. These findings establish a new paradigm: utilizing additive manufacturing not merely as a fabrication tool, but as a microstructural engineering method to govern the passivation dynamics and defect chemistry of advanced titanium alloys.

1. Introduction

Metastable beta-titanium (β-Ti) alloys are increasingly important because they uniquely combine beneficial characteristics, including low mass density, high strength-to-weight ratio, low stiffness (elastic modulus), and excellent responsiveness to hardening processes [1,2]. These qualities make them optimal materials for critical components in sectors like aerospace, high-performance engineering, and the biomedical industry [3]. Furthermore, compared to the α-phase and α + β titanium alloy families, β-Ti alloys offer enhanced workability and achieve better mechanical performance through specific thermo-mechanical or heat treatments [4]. This is primarily because the inherent stability of the β-phase allows for the resulting material properties to be precisely modified or 'tuned' by controlling the alloy's composition and manufacturing route [5,6].

Among metastable β-titanium alloys, Ti-21S (Ti-15Mo-3Nb-3Al-0.2Si) is recognized for its remarkable combination of elevated-temperature strength [7], creep resistance [8], corrosion resistance (particularly when exposed to aircraft hydraulic fluids) [9], and thermal stability [10]. This capability to sustain mechanical performance in demanding service environments stems from its composition. The alloys properties are fundamentally driven by the precise balance of its

* Corresponding authors at: Department of Management and Production Engineering, Politecnico di Torino, Corso Duca degli Abruzzi 24, Torino 10129, Italy.
E-mail addresses: amir.behjat@polito.it (A. Behjat), abdollah.saboori@polito.it (A. Saboori).

https://doi.org/10.1016/j.jallcom.2026.191961
Received 13 August 2026; Received in revised form 10 October 2026; Accepted 23 October 2026
Available online 24 October 2026
0925-8388/© 2026 The Authors. Published by Elsevier B.V. This is an open access article under the CC BY license (http://creativecommons.org/licenses/by/4.0/).

alloying elements, particularly the high molybdenum and niobium content, which stabilize the β- phase. Specifically, the inclusion of silicon additions [11] and potent β- stabilizing elements [12].

Consequently, Ti-21S is highly regarded for deployment in aerospace structures, heat-resistant parts, and applications involving chemically aggressive exposure [13]. Despite these compelling advantages, the alloy presents practical difficulties for conventional processing methods like forging or casting [14], primarily exhibiting limited weldability and poor thermal conductivity [15]. These inherent material characteristics create considerable obstacles to its fabrication.

Conventional fabrication techniques, including forging, casting, and welding, routinely encounter severe impediments when applied to β-titanium alloys like Ti-21S [8]. The alloys low thermal conductivity and inherent susceptibility to weld cracking significantly impede the successful production of components free from defects [16]. Furthermore, the materials high intrinsic strength necessitates extensive and complex machining, leading to increased production costs. These collective processing difficulties not only impose restrictions on design freedom but also inflate the overall manufacturing expense [17]. As a direct result, there is increasing scholarly and industrial interest in exploring advanced manufacturing technologies capable of overcoming these barriers to reliably produce high-performance Ti-21S components with optimized microstructural and mechanical characteristics.

Additive Manufacturing (AM), especially fusion-based techniques, provides significant advantages for creating intricate titanium components by reducing both material waste and production time [6,18–22]. The Laser Powder Directed Energy Deposition (LP-DED) process is highly prominent within this field [23], recognized for its rapid deposition rate, adaptability with various feedstocks, and ability to generate near-net-shape parts with controlled microstructures [24,25]. LP-DED's capacity for localized melting and solidification, which facilitates precise thermal gradient control, is particularly beneficial for alloys challenging to process using conventional methods, such as Ti-21S. This precise control mechanism is key to minimizing defects, optimizing microstructural development, and ultimately maintaining the alloy's inherent high-performance characteristics [25,26].

Studies in the open literature detailing the AM response of Beta 21S are largely limited to laser powder bed fusion (L-PBF) [10,27]. Despite the promising advantages of LP-DED, its application to the Ti-21S alloy remains scarce [28]. A recent study fabricated Beta 21 s with a laser power of 450 W, traverse speed of 6.35 mm/s, 1.14 mm hatch spacing, 0.4 mm layer height, and a powder flow rate of 0.55 g/s. The optimal sample exhibited a positive response to heat treatments, yielding microstructures analogous to those observed in wrought materials. The mechanical properties closely approximated those of wrought counterparts in terms of tensile strength; however, the tensile ductility was somewhat diminished [29]. However, a significant knowledge gap exists, particularly in understanding the direct relationship between LP-DED's adjustable processing parameters and the resulting microstructure, mechanical performance, and corrosion behavior of the final Ti-21S components [25,28].

Collectively, considering both the alloys substantial industrial relevance noted for its high temperature, creep, and oxidation resistance, and the inherent difficulties encountered in its conventional fabrication, such as low thermal conductivity and limited weldability [30,31], thorough investigation is essential to confirm the feasibility of using LP-DED for manufacturing high-quality Ti-21S parts. To address these technical challenges, this study moves beyond conventional parameter optimization to investigate the fundamental physical mechanisms governing microstructural evolution and surface passivation in LP-DED Ti-21S. Rather than merely identifying optimal processing parameters, the primary objective of this research is to establish a direct correlation between the rapid solidification kinetics inherent to LP-DED and the resulting defect chemistry of the protective oxide film. By utilizing the Point Defect Model (PDM), this work elucidates how the homogeneous β-matrix dictated by specific LP-DED thermal profiles fundamentally alters the oxygen vacancy concentration and semiconducting properties of the passive layer.

To support this mechanistic electrochemical investigation, the study concurrently evaluates the underlying melt pool thermodynamics, crystallographic evolution, and sub-micrometric mechanical responses of the fabricated components. Ultimately, the resulting insights demonstrate how the unique thermal history of LP-DED can be strategically leveraged not just to mitigate traditional fabrication constraints, but to actively engineer the passivation dynamics and multi-property performance of advanced metastable β-titanium alloys.

2. Materials and methods

2.1. Powder materials

The study utilized a pre-alloyed Ti-21S powder, obtained from ECKART TLS GmbH, as the feedstock for the LP-DED process. The particle size distribution of 45 μm to 105 μm was consistent with LP-DED requirements. Table 1 shows the composition as specified by the certificate of conformity provided by the supplier. The Mo equivalent (MoE) calculated by means of Eq. (1) highlights that this alloy is a metastable β Ti alloy since it occurs in the interval between 10 and 30 wt % [10].

$$MoE = 1.0(wt\%\ Mo) + 0.67(wt\%\ V) + 0.44(wt\%\ W) + 0.28(wt\%\ Nb) + 0.22(wt\%\ Ta) + 2.9(wt\%\ Fe) + 1.6(wt\%\ Cr) + 1.25(wt\%\ Ni) + 1.70(wt\%\ Mn) + 1.70(wt\%\ Co) - 1.0(wt\%\ Al). \quad (1)$$

The morphology of the powder particles was analysed using a scanning electron microscope (SEM, Philips XL) fitted with an energy-dispersive X-ray spectrometer (EDS). Prior to deposition, the powder was prepared to ensure purity and optimal handling. It was dried at 80 °C for 2 h to eliminate moisture, and stored in sealed, argon-filled containers to prevent oxidation.

2.2. Sample fabrication and preparation

The LP-DED Additive Manufacturing system employed for the research was a SUPSI-developed Laserdyne 430 machine equipped with a Convergent Photonics CF1000, operating at a maximum laser power of 1000 W and showing a wavelength of 1070 nm and a 1 mm laser spot. The machine featured a multi-nozzle deposition head (Optomec Inc., USA) connected with a volumetric powder feeding system (rotating disc-type Optomec LENS engine, USA). Powder delivery was managed by a single-hopper feeding system set at 1 RPM, corresponding to a mass flow rate of 1.02 g/min, An inert argon (Ar) atmosphere, supplied via carrier and shielding gas, was maintained throughout the build to prevent oxidation. Samples were fabricated in a cubic geometry (20 mm× 20 mm × 10 mm) using a raster scanning strategy with alternating 0°/ 90° layer rotations to minimize residual stress accumulation. The deposition experiments were conducted on a Ti-6Al-4V substrate with dimensions of 200 × 100 × 10 mm^3 . Prior to deposition, the substrate was preheated to 200 °C to reduce the thermal gradient between the substrate and the deposited material. The substrate was maintained at the specified preheating temperature during the deposition process. The deposited structure had a nominal height of 10 mm, which corresponds to the height of the deposited Ti–15Mo–3Al–3Nb–0.2Si alloy and excludes the thickness of the substrate.

The core process parameters including laser power, scanning speed, layer height, and hatch distance are detailed in Table 2. In this table, H. D. denotes hatch distance (mm), and dz denotes layer thickness (μm)

Table 1
Chemical composition (wt%) of the pre-alloyed Ti-21S powder used as feedstock in the LP-DED process.

Element	Ti	Mo	Al	Nb	Si	O	C	N
Ti-21S	Bal.	15	3.2	2.7	0.2	0.17	0.05	0.05

Table 2
Optimized LP-DED parameters for the fabrication of Ti-21S samples.

Sample Number	Power (W)	Speed (mm/min)	H.D (mm)	dz (μm)	Line Energy (J/mm)	Raster
N.1	400	600	0.479	186	40	0°/ 90°
N.2	400	500	0.501	151	47	0°/ 90°
N.3	500	600	0.589	170	50	0°/ 90°
N.4	500	500	0.605	201	60	0°/ 90°

(step height per layer). These parameters were systematically varied and optimized by identifying the ideal liner density required to ensure a stable melt pool. Upon completion, Samples were detached from the build plate using a BAOMA BMW-3000 Wire Cutting WEDM system, ensuring precise sectioning without inducing mechanical deformation or thermal damage to the LP-DED microstructure. A schematic illustration of the Ti-21S alloy fabricated via LP-DED, manufacturing system used for deposition, the designated areas for characterization, accompanied by the experimental analyses conducted in this study, are shown in Fig. 1.

To provide a more physical and comparative basis for analyzing the experimental results, the samples are categorized and discussed hereafter based on their specific Line Energy (L.E.) values rather than their initial sample numbers (N.1–N.4). These values were calculated according to Eq. (2) as detailed in Table 2, the Line Energy values calculated from the laser power and scanning speed from 40 to 60 J/mm. Since this parameter directly influences the thermal history and energy density during the LP-DED process, it serves as the primary variable for evaluating and presenting the subsequent findings in microstructure, mechanical properties, and corrosion resistance. It was worth to be mentioned that this parameter serves as a useful one-dimensional metric to compare relative thermal inputs, it does not fully capture the three-dimensional volumetric variations resulting from simultaneous adjustments to hatch distance and layer height.

$$\text{L.E.} = \frac{P}{V}\left(J \Big/ mm\right) \quad (2)$$

As a baseline reference, LP-DED Ti6Al4V specimens exhibiting an acicular alpha phase alongside a minor beta microstructure were fabricated under optimized processing conditions [32].

2.3. Defect analysis

The density and porosity of the LP-DED samples were assessed using Archimedes principle in accordance with ASTM C373. A high-precision analytical balance (KERN ABS-N, readability 0.1 mg) was used to measure the mass of each specimen in air and when immersed in deionized water at 24 °C. The theoretical density of Ti-21S (4.94 g/cm^3) was adopted for calculating relative density [10]. All measurements were performed in triplicate. The bulk density was determined using this approach, which provided a reliable quantification of densification and allowed comparison across different process conditions.

To validate and complement the Archimedes density results, high-

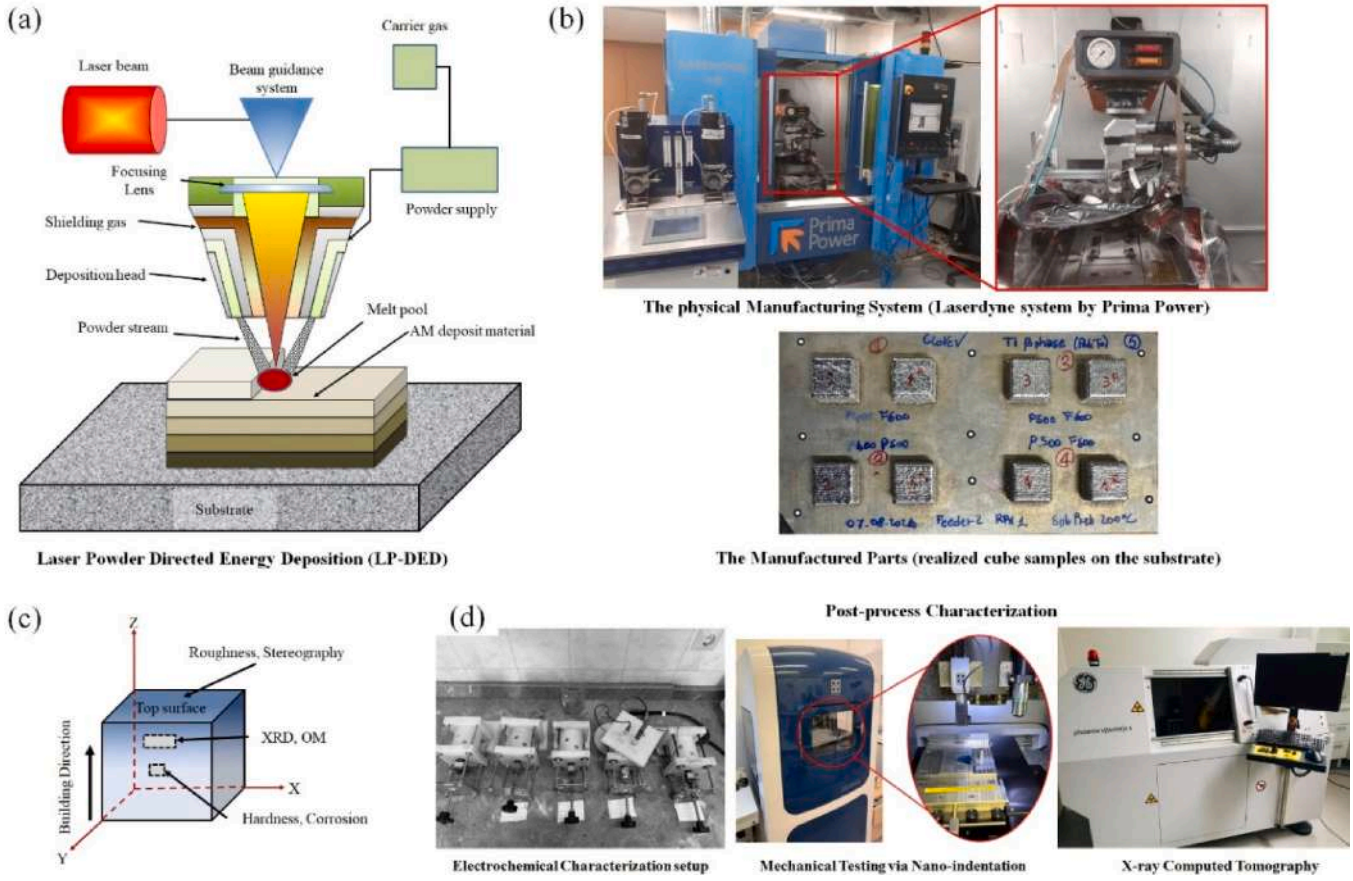


Fig. 1. Comprehensive workflow of the additive manufacturing process and subsequent characterization, (a) Schematic representation of the LP-DED mechanism highlighting the interaction between the laser beam, powder stream, and melt pool, (b) The Laserdyne manufacturing system used for deposition and realized titanium-based samples demonstrating the printed geometry, (c) A diagram of the cube sample showing the reference system and the specific regions selected for microstructural analysis as well as for hardness and corrosion testing, and (d) Multi-scale characterization techniques conducted in this study.

resolution X-ray Computed Tomography (X-CT) was performed using a GE Phoenix v|tome|x S micro-CT scanner, with data acquisition conducted at a voltage of 240 kV and a current of 110 μA, achieving an effective measurement resolution (voxel size) of 20 μm. CT reconstruction enabled visualization and quantification of internal defects. To reduce beam hardening artifacts, physical filters composed of copper and tin, each measuring 0.5 mm in thickness, were employed. The sample was subjected to a full 360° rotation, during which 1600 projections were acquired at angular increments of 0.225°, with an exposure duration of 1 s per projection, using a charge-coupled device (CCD) detector. The acquired CT projections were subsequently processed utilizing VGStudioMax version 3.4. This software was also used for the reconstruction of the three-dimensional volume, followed by porosity analysis conducted after the external surface of the scanned specimens was delineated.

2.4. Roughness and surface morphologies

Surface roughness was characterized using a stylus profilometer (RTP80–TL90, Someco SM SRL.). Measurements were performed at three distinct positions (left, center, and right) on the top surface of each sample. The measurement path was oriented perpendicular to the final laser scanning tracks to capture the most significant topographic variations. To separate the roughness profile from waviness and form error, a Gaussian filter with a cutoff length of 0.8 mm was applied, in accordance with ISO 4288 standards for expected roughness in LP-DED processes. Profile-based parameters Ra, Rz, and Rt were calculated and averaged across all three positions to ensure statistical representation of the surface quality for each processing condition. Specifically, Ra was used to represent the global average roughness, while Rz (mean peak-to-valley height) and Rt (total height) were analyzed to identify extreme surface irregularities or balling effects characteristic of unoptimized energy density.

In addition to quantitative roughness measurements, stereo optical microscopy was used to qualitatively examine the surface morphology of the LP-DED samples. Imaging was conducted using a Leica M205C stereo microscope equipped with a high-resolution digital camera. This system provides high-contrast depth imaging, allowing visualization of melt track patterns, and surface texturing associated with different parameter sets.

2.5. Microstructure analysis

Phase analysis was performed using a Bruker XRD diffractometer with Cu Kα radiation (λ = 1.5406 Å), operating at 50 kV and 30 mA, over a 2θ range of 20°–100°. To comprehensively examine the microstructure of samples, analyses were conducted along the building direction (BD) using optical and electron microscopy techniques. Prior to microstructure analysis, samples were subsequently ground using SiC abrasive papers from 800 up to 2400 grit and polished using 3 μm and 1 μm diamond suspensions on a PRESI Minitech 250 SP1 automatic polishing system. A final polishing step with colloidal silica was performed to produce a deformation-free mirror surface suitable for high-resolution microstructural examination. Chemical etching was carried out using Kroll's reagent (2% HF, 6% HNO_3, 92% H_2O) for 8–13 s to reveal grain boundaries, melt pool geometry, and β-phase features. Optical microscopy was performed using a Leica DM2700 M metallurgical microscope, which allowed observation of melt pool morphology, remelting regions, and grain growth patterns associated with the LP-DED thermal cycles. The quality of the printed specimens was evaluated utilizing a MIRA3-TESCAN SEM. The SEM system was additionally coupled with energy-dispersive spectroscopy (EDS) to facilitate elemental analysis.

2.6. Hardness measurements

Mechanical properties were evaluated using Vickers microhardness testing and nanoindentation. Microhardness was measured on the polished top surface using a Vickers hardness tester (KOOPA UV1) according to ASTM E92, applying a load of 200 mg for 15 s. A total of 5 indents were placed on each specimen along building direction plane, with sufficient spacing to avoid interaction between plastic zones. Nanoindentation tests were performed on polished samples at room temperature using a Hysitron TI 950 TriboIndenter® (Bruker Nano Surfaces, USA) equipped with a Berkovich tip. Before nanoindentation experiments, the nanoindenter device was calibrated by a reference sample of fused silica to get accurate results. A matrix of 3 × 3 indents was applied under a maximum load of 7000 μN, loading rate of 50 μN/s, and dwell time of 10 s. The resulting load–displacement curves were used to extract hardness and reduced modulus using the TriboScan™ software and Oliver-Pharr method.

2.7. Electrochemical measurements

Electrochemical experiments were carried out in a conventional three-electrode cell system in 0.9 wt% NaCl solution at 25°C by using a potentiostat (1000/Gamry Device). Before electrochemical measurements, the samples were ground with SiC papers from 80 to 1200 grits. Tests were carried out in a solution using a three-electrode configuration consisting of the sample as working electrode, a platinum mesh counter electrode, and an Ag/AgCl reference electrode. The open-circuit potential (OCP) experiments were performed to obtain stability between the solution and the surface. EIS measurements were performed under OCP conditions after different immersion times (1, 3, 24 and 144 h over a frequency range from 100 kHz–0.01 Hz with a 10 mV perturbation amplitude. Mott-Schottky (MS) analysis was performed to determine the semiconducting characteristics of the passive film. The measurements were conducted at a frequency of 1 kHz, employing a 10 mV AC perturbation and a potential step size of 10 mV. The applied potential was progressively decreased in the cathodic direction, starting from an initial value of 1.0 V versus Ag/AgCl and ending at −1.0 V versus Ag/AgCl. Prior to the MS measurements, the samples were allowed to stabilize at their corrosion potential. All electrochemical experiments were repeated a minimum of three times to ensure reproducibility. As shown in Fig. 1(c), all microhardness indents, nanoindentation arrays, and electrochemical corrosion tests were performed on longitudinal X-Z along B.D cross-sections extracted consistently from the mid-height region (4–6 mm from the substrate interface) of the 10 mm cubic builds.

3. Result and discussion

3.1. Feedstock characterization

Fig. 2 shows the SEM micrograph and particle size distribution of the Ti-21S feedstock powder. The particles exhibit a predominantly spherical morphology with smooth surfaces, which is characteristic of argon gas-atomized β-Ti powders [33]. Only a limited number of fine satellites are observed on the surface of larger particles, indicating good atomization quality and high powder flowability [34]. Fig. 2(a) displays the outcomes of the EDS mapping analysis performed on the initial powder. The measured chemical compositions were found to fall within the acceptable limits established for wrought counterparts. This analysis was conducted to examine the surface properties of the powder, as well as to assess the extent of oxidation and the uniformity of its chemical composition. As depicted in Fig. 2(a), the particle size distribution of the powder with a D10, D50 and D90 of 48 μm, 83 μm and 104 μm, respectively. Furthermore, the spherical shape and narrow size distribution are expected to promote stable powder delivery and homogeneous melting during LP-DED, thereby supporting the high densification measured later [35,36].

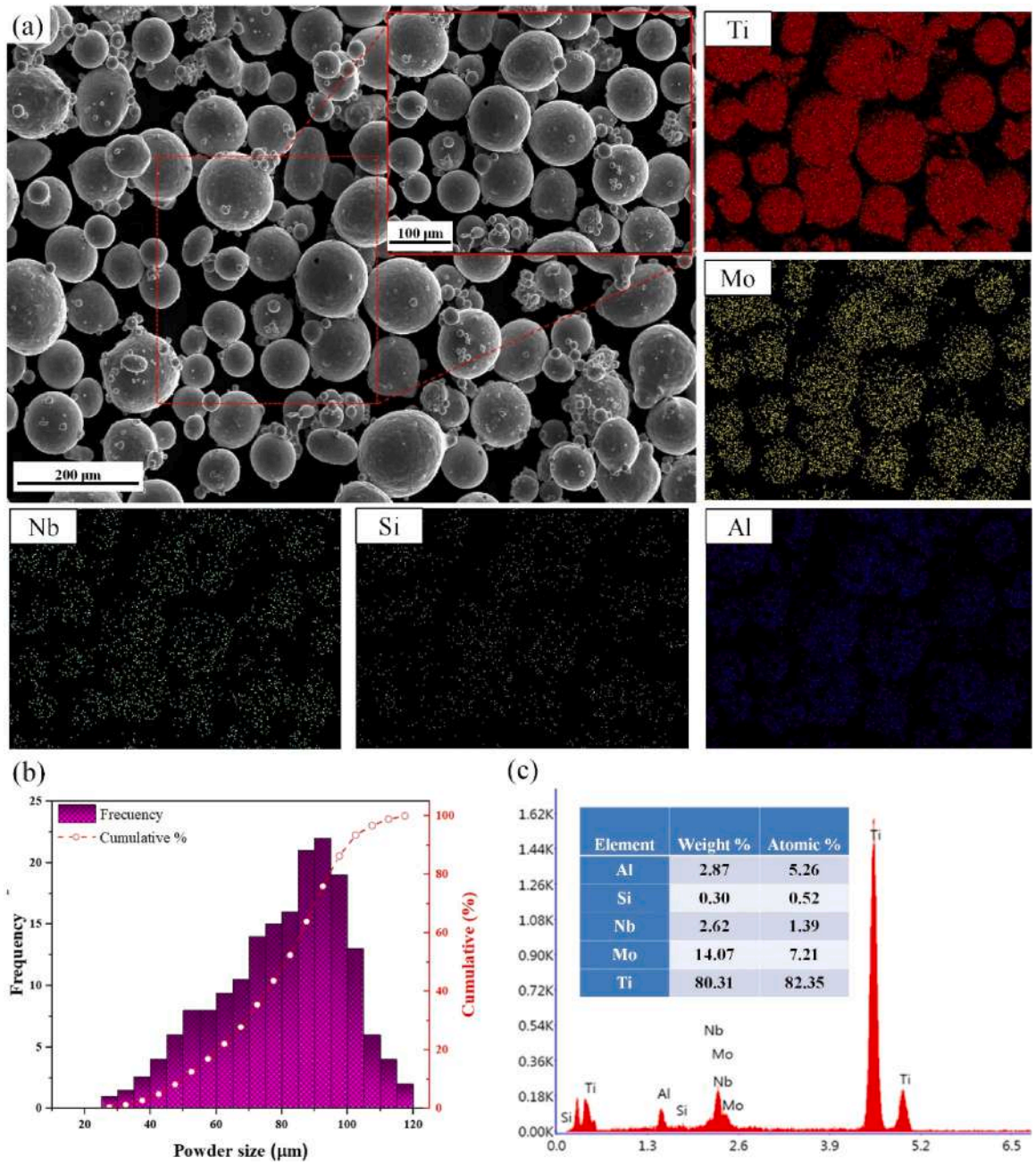


Fig. 2. Powder characterization (a) SEM image and EDS map of the powders, (b) particle size distribution and, (c) EDS analysis of the powders.

3.2. Densification Behavior and Defect Characteristics

Rather than merely identifying the operational parameters for high densification, the interaction between the laser L.E. and the Ti-21S powder was analyzed to map the hydrodynamic stability of the melt pool. The relative density and porosity of the LP-DED Ti-21S samples were quantified using Archimedes principle (ASTM C373) and validated through cross-section analyses and high-resolution X-ray computed tomography (CT) [37]. The Archimedes measurements, performed in triplicate for each specimen, revealed that all samples exhibited relative densities exceeding more than 99%, indicating a high level of densification achieved under the selected processing parameters. Minor variations between samples reflected the influence of changing laser power, scanning speed, and hatch distance across the four fabrication conditions. The calculated density values showed close agreement with the theoretical density of Ti-21S (4.94 g/cm^3), and the overall porosity content remained below 1% for all specimens; the results of this section are shown in Table 3. These low porosity levels are consistent with effective energy input, stable powder delivery, and proper melt pool formation during LP-DED deposition [38].

To validate these results, cross-sectional analysis with optical microscopy and micro-CT scans was conducted on representative samples using a GE Phoenix v|tome|x S system. The three-dimensional tomography reveals the spatial positioning and morphology of pores. As

Table 3
Relative Density of LP-DED Ti-21S samples as a function of Line Energy.

L.E. (J/mm)	Density [g/cm^3]	Relative Density [%]	STDEV
40	4.93	99.87	0.1026
47	4.93	99.69	0.0152
50	4.93	99.74	0.1026
60	4.94	99.91	0.0513

depicted in Fig. 3, reconstructed 3D volumes confirmed the absence of large lack-of-fusion (LoFs) defects or interconnected pore networks. The observed pores were predominantly spherical and smaller than 50 μm, characteristic of gas-entrapped porosity rather than process-induced imperfections [21]. The homogenous spatial distribution of these pores further supports the stability of the LP-DED process. Additionally, the two-dimensional computed tomography images corroborate a uniform pore distribution within the dense samples.

Bulk density evaluated via Archimedes principle and internal pore fractions quantified via micro-CT ($\geq$ 20 μm resolution) showed excellent general agreement, with minor numerical variations reflecting the different measurement scales and detection thresholds of each technique. The combination of Archimedes analysis and micro-CT inspection conclusively demonstrated the high densification and structural integrity of the LP-DED Ti-21S builds. This observation indicates that the process settings successfully suppressed critical defect types such as elongated lack-of-fusion pores, which are known to compromise fatigue performance. These results ensure reliability in correlating subsequent microstructural, mechanical, and electrochemical evaluations with the employed processing parameters. The overall porosity fraction across all conditions ranged between 0.1% and 0.25%, with the lowest values recorded in samples with L.E 60 J/mm corresponding to those with the highest measured densities. Importantly, no evidence of significant pore clustering was detected, suggesting uniform powder spreading and stable energy input throughout the build process.

Fig. 4 presents the distributions of pore diameter and sphericity for the fabricated samples. The findings offer critical insights into the influence of varying L.E. values on pore morphology, relative density, and the overall quality of components produced via LP-DED. As illustrated, the sample processed with an L.E. of 50 J/mm exhibits a narrower pore size distribution and higher sphericity, indicating more uniform and controlled porosity. This specific energy input facilitates the formation of a stable melt pool, thereby minimizing pore generation and improving the structural homogeneity of the manufactured components.

The non-monotonic density trend observed across the processing window is driven by the transition from incomplete consolidation to a fully stable fluid flow. At lower energy inputs (40–47 J/mm), the density is limited by LoF porosity, where the melt pool is too narrow to bridge the hatch distance, leaving irregular, jagged voids as seen in the low-sphericity clusters of plots as depicted in Fig. 4. At 50 J/mm, the material enters a transitionary instability phase; the increased heat creates a deeper, more turbulent melt pool that can intermittently trap shield gas, resulting in the localized drop in density to 99.81% and the appearance of larger, more prominent pores. The peak density of 99.89% at 60 J/mm is achieved because the higher thermal input promotes superior Marangoni convection and a longer liquid lifetime. This allows for better wetting of the substrate and provides sufficient time for any entrapped gas bubbles to rise and escape before solidification. Consequently, the remaining pores at 60 J/mm are exclusively small and highly spherical, signifying that the process has reached an optimal steady-state where LoF is eliminated without yet entering the aggressive keyhole regime characterized by metal vaporization.

3.3. As-built surface roughness

Fig. 5(a) shows the stereo images of samples according to the L.E., where clear variations in melt-track geometry, bead overlap, and surface waviness are observable. L.E. = 40 J/mm and L.E. = 47 J/mm exhibit more uniform and aligned melt-track patterns, whereas L.E. = 50 J/mm and L.E. = 60 J/mm present higher levels of irregularity and undulation. These qualitative differences indicate the sensitivity of surface formation to changes in energy input and melt-pool dynamics.

Quantitative surface roughness measurements performed using profilometer further support the qualitative observations. Fig. 5(b,c) and Table 4 present the Ra, Rz, and Rt parameters for all samples. Among the analyzed specimens, the lowest roughness Ra = 8.12 ± 0.82 μm) was achieved at of 47 J/mm. At this optimal energy threshold, the laser provides sufficient enthalpy to fully melt the powder and wet the underlying substrate, allowing surface tension to smoothly spread the liquid metal before solidification. Conversely, at the highest energy input (L.E. 60 J/mm) the roughness degrades severely Ra = 18.86 ± 1.82 μm). The intense energy density causes localized boiling of the titanium alloy, generating intense metal vapor plumes. The resulting recoil pressure depresses the melt pool, creating a deep capillary cavity. This highly unstable dynamic induces violent Marangoni convection, causing the melt pool walls to collapse and ejecting molten spatter onto

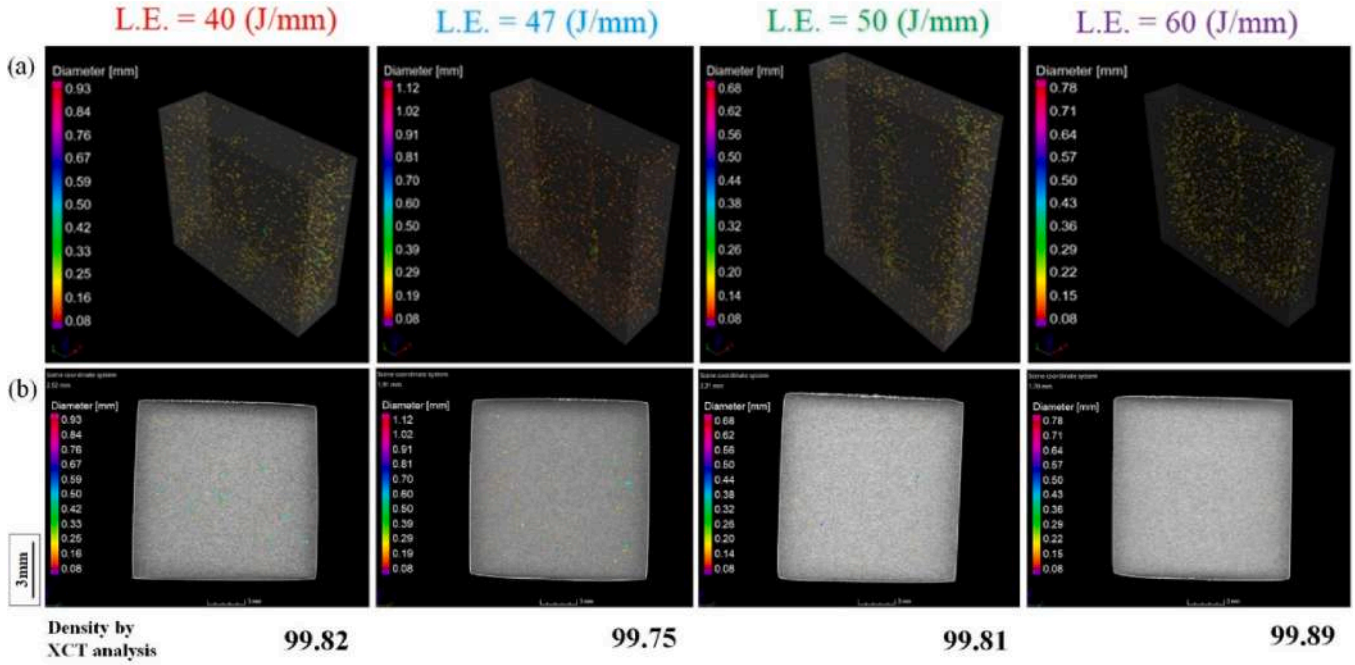


Fig. 3. The analysis of the relative density of the samples is presented as follows: (a) illustrates the three-dimensional tomography, while (b) highlights the frontal view of the samples, revealing internal features through tomographic imaging.

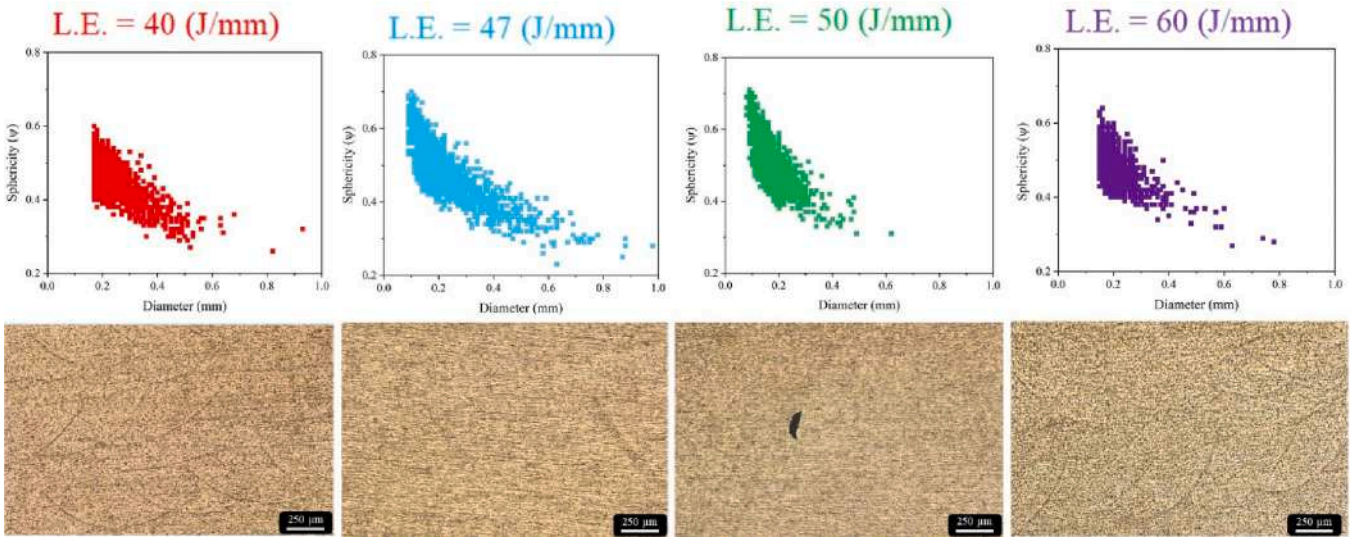


Fig. 4. Pore diameter and sphericity distribution for samples with corresponding OM images.

the surrounding surface. Furthermore, extreme thermal gradients cause the solidifying track to ripple and undulate, resulting in the massive (Rt) values observed.

To provide additional insight, Fig. 5(c) illustrates the longitudinal roughness profiles extracted from each sample. The profiles reveal substantial differences in the amplitude of surface fluctuations L.E. = 40 J/mm shows the smallest peak variations and the most stable progression along the scanned length. L.E. = 47 J/mm exhibits moderate irregularities, with occasional sharp fluctuations corresponding to localized defects or unmolten particle traces. L.E. = 50 J/mm displays larger periodic oscillations, likely associated with melt-pool instability or increased hatch-dependent track curvature. L.E. = 60 J/mm presents the highest peak intensities, confirming the presence of significant surface asperities and suggesting excessive melt-track height variation. Overall, the combined qualitative and quantitative analyses indicate a clear correlation between LP-DED processing parameters and the resulting surface quality. Lower roughness values are associated with more stable thermal regimes and optimized bead overlap, whereas higher roughness is linked to insufficient melt-pool stability, excessive heat input gradients, or suboptimal hatch spacing. This trend is consistent with the visual inspection of the stereo images, where Sample L.E. = 60 J/mm displays pronounced peak-to-valley fluctuations, reflecting unstable melt-pool solidification or insufficient overlap during deposition. Indeed, higher energy extend the liquid lifetime and enhance fluid spreading to eliminate LoF defects, they simultaneously induce intense metal vaporization, recoil pressure fluctuations, and Marangoni convection instabilities that degrade the top-surface finish.

Collectively, these findings demonstrate that an energy threshold between 50 and 60 J/mm fundamentally stabilizes Marangoni convection and extends the liquid lifetime. This thermodynamic stability successfully suppresses LoFs defects and localized spatter, thereby providing a flawless, chemically isotropic beta-matrix essential for the subsequent fundamental evaluation of its electrochemical defect structure. These findings serve as a basis for linking surface morphology with microstructural evolution and subsequent mechanical performance, espicialy surface asperities provide localized notch sites that dictate fatigue initiation and surface-area discrepancies during post-processing. In following investigation based on standard, polished samples were used for microstructural and electrochemical testing, characterizing as-built surface roughness establishes the process-window limits for high-deposition-rate LP-DED, defining operational tolerances for near-net-shape manufacturing.

3.4. Microstructure Analysis

In LP-DED, the microstructural architecture is strictly governed by the extreme, localized ratio of the thermal gradient (G) to the solidification rate (R). To understand the physical origins of the alloy's mechanical response, the influence of these directional thermal cycles on the crystallographic retention of the metastable beta-phase was investigated. Fig. 6 presents the X-ray diffraction patterns of the Ti-21S precursor powder and the LP-DED fabricated samples (L.E. = 40 – 60 J/mm). All XRD patterns exhibit reflections corresponding exclusively to the body-centered cubic (bcc) β-titanium phase, with the main peaks located at approximately 38.9° (110), 55.0° (200), 69.0° (211), 82.5° (220), and 98.0° (310). The absence of α-Ti, ω-Ti, or intermetallic reflections indicates that the rapid solidification conditions inherent to LP-DED effectively retain the metastable β phase throughout the fabricated parts.

A comparison between the feedstock powder and the deposited samples reveals notable differences in peak morphology. The powder spectrum displays broader and lower-intensity peaks, particularly for the (110) reflection, which is characteristic of fine crystallite size and internal strain generated during gas atomization. In contrast, all LP-DED samples exhibit sharper and higher-intensity diffraction peaks, signifying reduced micro strain, grain coarsening, and enhanced crystallinity following melting and solidification.

The influence of L.E. on the crystallographic characteristics of the LP-DED Ti-21S alloy was evaluated through a detailed analysis of the beta (110) diffraction peak. A magnified view of the (110) peak highlights a subtle shift toward lower 2θ values for all fabricated samples relative to the powder. As summarized in Table 5, a clear correlation exists between the energy input and the resulting lattice parameters. As the linear energy increased from 40 J/mm to 60 J/mm, the Full Width at Half Maximum (FWHM) exhibited a progressive decrease from 0.44 to 0.39. According to the Scherrer relationship, the observed narrowing of the diffraction peak corresponds to an increase in the XRD-derived crystallite size from 24 to 35 nm as the line energy increased from 40 to 60 J/mm. It should be noted that this parameter represents the approximate coherent diffraction domain size and should not be directly interpreted as the metallographic grain size. The observed increase in crystallite size is consistent with the reduced microstrain and the increased thermal exposure associated with higher energy input, which may promote recovery and structural relaxation during the successive thermal cycles of the LP-DED process. Consequently, strengthening is interpreted through dislocation density and sub-grain boundary spacing rather than classic

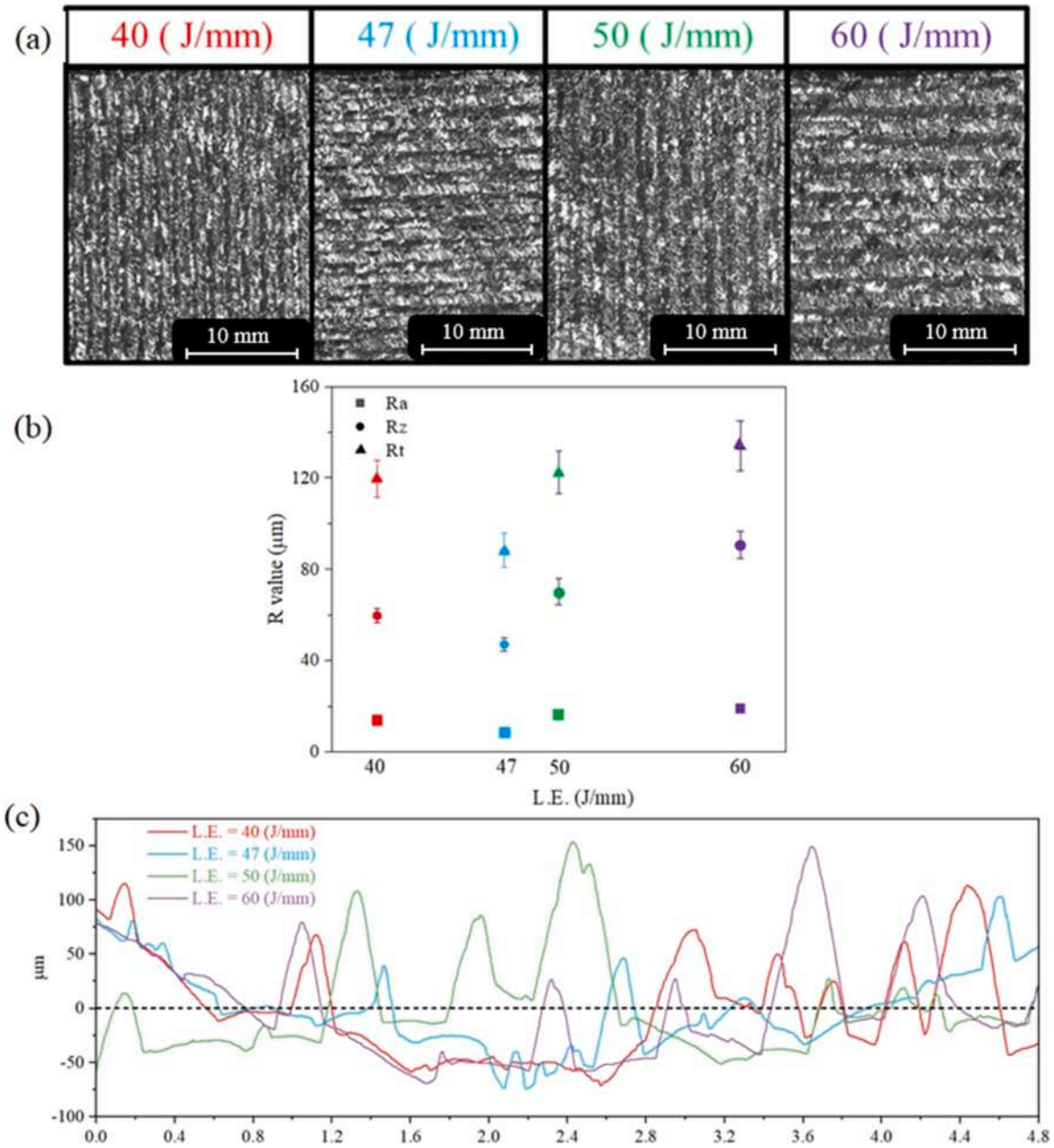


Fig. 5. Comprehensive surface roughness analysis, (a) Stereo optical micrographs of the as-deposited top surfaces of Ti-21S samples, (b) summary of R-values relative to L. E., and (c) representative longitudinal surface profiles.

Table 4
Statistical summary of surface roughness parameters (Ra, Rz, and Rt) for LP-DED Ti-21S specimens.

L.E. (J/mm)	40	47	50	60
Ra	13.72 ± 1.25 μm	8.12 ± 0.82 μm	16.21 ± 1.35 μm	18.86 ± 1.82 μm
Rz	59.62 ± 3.11 μm	46.99 ± 2.77 μm	70.12 ± 5.72 μm	90.54 ± 6.04 μm
Rt	119.54 ± 8.05 μm	88.27 ± 7.43 μm	122.25 ± 9.26 μm	133.96 ± 11.03 μm

Hall-Petch grain boundary hardening.

According to the Scherrer relationship, this narrowing of the diffraction peak signifies a notable increase in the average crystallite size, which grew from 24 nm to 35 nm. This trend is attributed to the higher peak temperatures and reduced cooling rates associated with elevated energy densities, which provide sufficient thermal energy for grain boundary mobility and subsequent crystallite coalescence.

Concurrently, the lattice microstrain generally followed a downward trend, decreasing from 0.32 to 0.25 at the highest energy level. In the context of LP-DED, lower energy inputs are characterized by extremely rapid solidification and steep thermal gradients, which trap high densities of dislocations and point defects within the metastable beta lattice. hence, This shift is indicative of slight lattice expansion, which may arise from residual tensile stresses generated during rapid thermal cycling or from increased dissolution of β-stabilizing elements such as Mo and Nb into the β-Ti lattice during the melt pool process [39]. The observed reduction in microstrain at higher L.E. values suggests an in-situ annealing effect, wherein the successive heat cycles from overlapping laser passes promote structural relaxation and the recovery of lattice distortions.

The peak positions (2θ) remained relatively stable between 38.94°

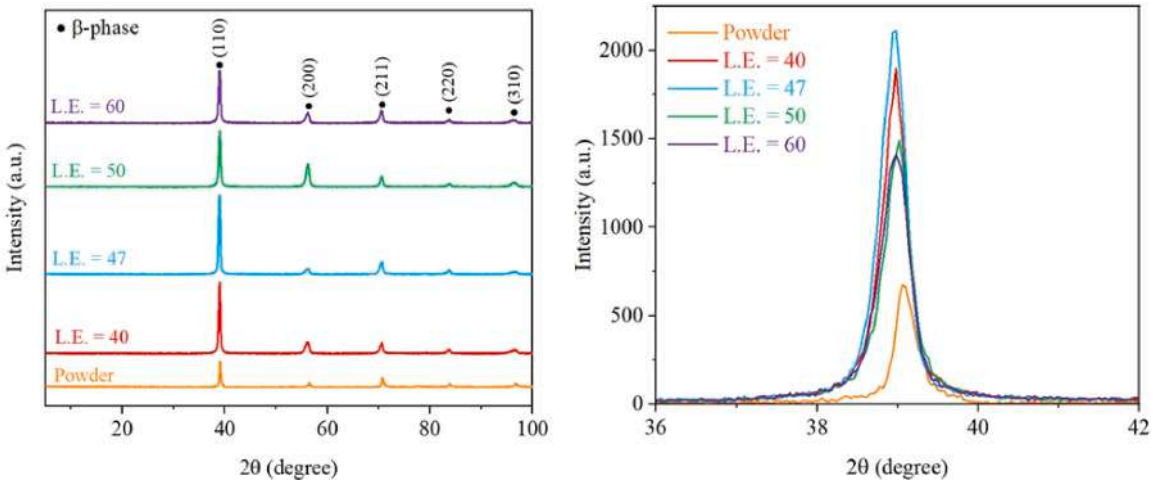


Fig. 6. XRD patterns of the initial powder and as-built-Ti-21S.

Table 5
XRD-derived analysis for LP-DED Ti-21S samples.

L.E. (J/mm)	40	47	50	60
2 θ	38.98	38.94	39.02	38.98
FWHM (110) peak	0.44	0.42	0.40	0.39
Crystal Size (nm)	24	27	32	35
Micro strain	0.32	0.34	0.29	0.25

and 39.02°, indicating that the fundamental beta-phase crystal structure was preserved across the processing window. However, the slight fluctuations in 2θ likely reflect localized variations in residual stress or minor solute redistribution within the melt pool. Collectively, these XRD results demonstrate that optimizing the energy density is critical not only for achieving high relative density but also for tailoring the internal stress state and crystallographic scale of the fabricated Ti-21S components.

However, the discussion of the microstructure must extend beyond

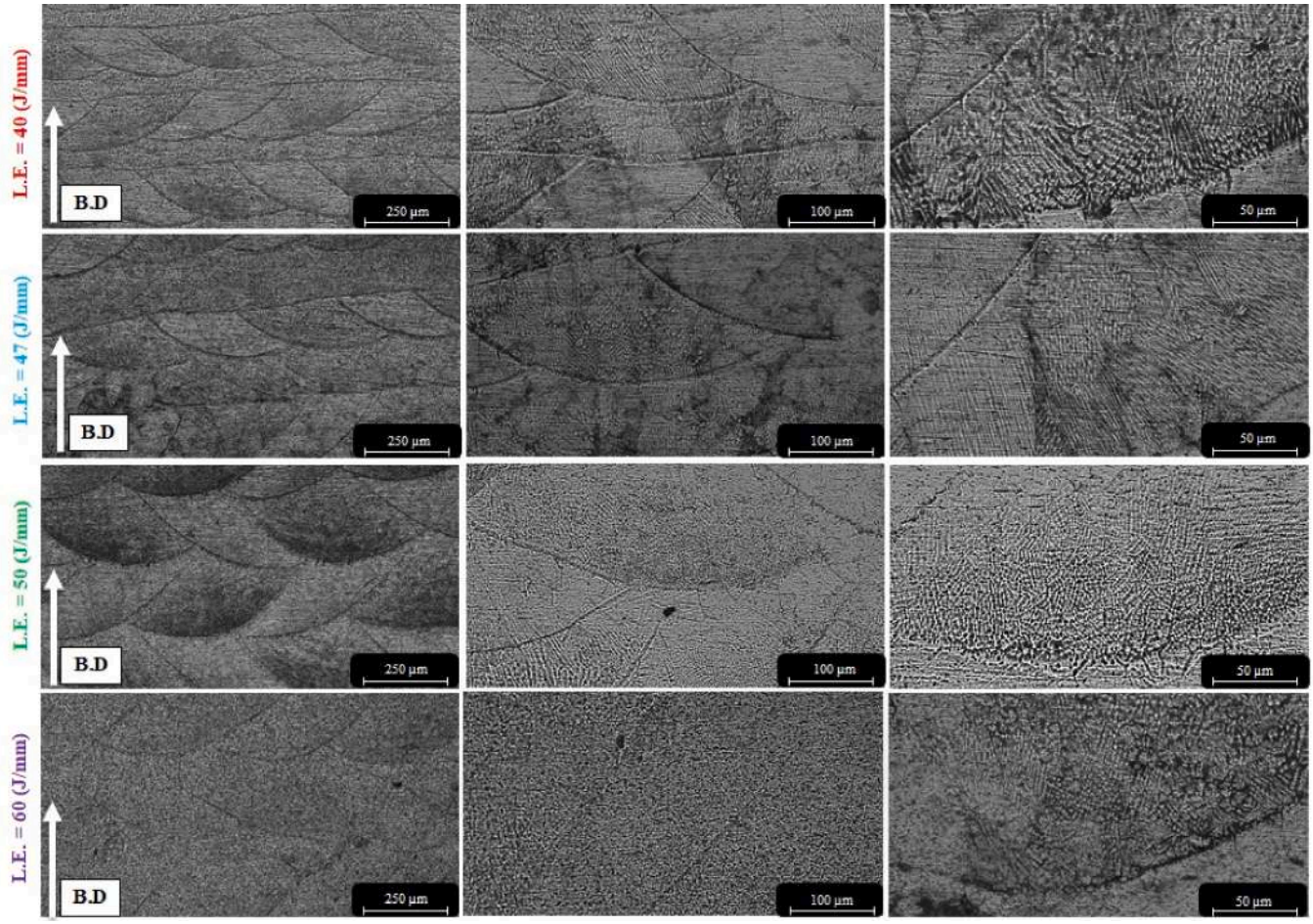


Fig. 7. Cross-sectional optical micrographs of as-built Ti-21S samples.

phase identification to address grain morphology and crystallographic texture. Fig. 7 presents the OM images of the LP-DED Ti-21S samples produced under four processing conditions. All samples display the typical LP-DED melt-pool architecture, consisting of overlapping semi-circular tracks that reflect the raster scan strategy and layer-by-layer remelting [40]. The melt pools are continuous and well-bonded, suggesting stable deposition and good metallurgical continuity across track boundaries. Samples L.E. = 40 J/mm and L.E. = 47 J/mm show clearly distinguishable melt-pool contours and regular overlap. L.E. = 60 J/mm exhibits finer and more homogeneous melt-pool features, indicating a more stable thermal regime or higher effective energy density. Moving to higher magnification, the microstructure within melt pools appears fully β-phase with fine cellular/sub-grain contrast, consistent with rapid solidification in metastable β-Ti alloys. No macroscopic cracks or large lack-of-fusion regions are visible, aligning with the near-full density reported from Archimedes/CT.

A qualitative comparison among parameter sets indicates that thermal input affects melt-pool geometry and local refinement, conditions producing slightly larger, more distinct pools (L.E. = 40 – 50 J/mm) point to stronger track-wise thermal gradients, whereas the smoother, more uniform field in L.E. = 60 J/mm suggests more even heat distribution and remelting. This trend is expected to influence hardness and corrosion behavior, which will be discussed in the subsequent sections.

It is important to note that AM processes are characterized by pronounced, directional thermal gradients (G). The grain morphology is governed by the ratio of the temperature gradient to the solidification rate (G/R) [41,42]. In LP-DED, the elevated G/R ratio at the melt pool boundary significantly promotes the growth of columnar grains. Additionally, due to the partial remelting of the previously deposited layer, grain nucleation occurs epitaxially, proceeding directly from the existing crystal lattice without requiring an activation energy barrier [43]. Consequently, this leads to the formation of extensive, highly oriented columnar beta grains that span multiple build layers and exhibit a strong alignment parallel to the build direction [44,45].

The cross-sectional SEM micrographs and corresponding EDX elemental mapping of the as-built Ti-21S alloy synthesized are presented in the Fig. 8. Observed along the B.D., the low-magnification SEM images exhibits the classic periodically stacked, fish-scale-like melt pool morphology characteristic of the layer-by-layer deposition process. At lower heat inputs (L.E. = 40 and 47 J/mm), the high G and rapid R induce the formation of fine, isotropic cellular-dendritic substructures within the interior of the melt pools. Conversely, increasing the linear energy to 50 and 60 J/mm alters the solidification thermodynamics, decreasing the G and R cooling rate. This promotes significant grain coarsening, a transition in grain morphology, and more pronounced epitaxial grain growth across the fusion boundaries due to the cyclic reheating and intrinsic heat treatment (IHT) effects of successive laser passes.

Recent studies on L-PBF metastable beta-titanium alloys of identical nominal composition (Ti-15Mo-3Al-2.7Nb-0.2Si) have revealed that laser-based manufacturing inherently triggers multiscale spinodal decomposition ($\beta \rightarrow \beta_1 + \beta_2$) driven by rapid thermal cycling and localized chemical fluctuations. Unlike conventional quenching routes, the unique thermal-defect history of laser additive manufacturing promotes uniform nanoscale compositional modulations that act as distributed speed bumps rather than hard barriers to dislocation motion. This microstructural phenomenon triggers the formation of serrated dislocations and high-density dislocation loops during deformation,

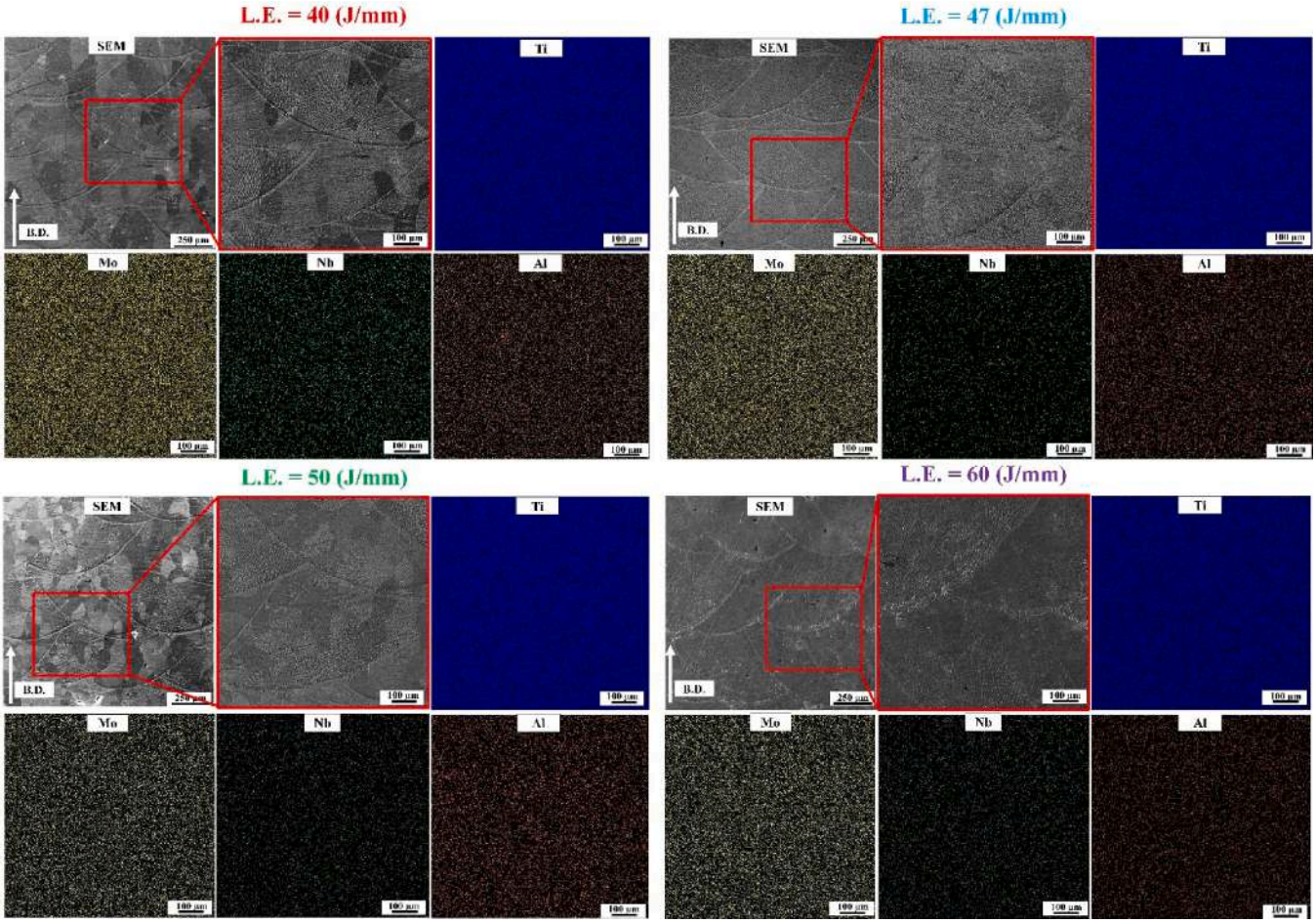


Fig. 8. SEM-EDX map for as-built Ti-21S samples.

effectively reconciling the traditional strength-ductility trade-off by promoting homogeneous plastic flow [46].

High-resolution EDX area-mapping was executed to evaluate the micro-segregation behavior of the primary alloying elements. LP-DED process successfully preserves the inherent chemical homogeneity of the pre-alloyed powder without causing macro-segregation or solute partitioning during rapid solidification. No discernible macroscopic solute segregation, chemical partitioning at the solidification fronts, or unmelted elemental powder clusters are observed across the investigated energy density spectrum. This exceptional chemical homogeneity confirms that the selected linear energies provided a sufficient thermal budget and hydrodynamic Marangoni convection within the molten pool to achieve complete solute diffusion, effectively yielding a macroscopically uniform elemental distribution beta-stabilized solid solution matrix in the as-built state.

It is noteworthy that, according to the aforementioned results, XRD analysis, within its detection threshold of approximately 1–2 vol%, along with SEM imaging, identified a predominantly retained beta-phase microstructure without observable secondary alpha-phase reflections. Nevertheless, the existence of sub-microscopic or nanoscale precipitates below the resolution limit of XRD cannot be conclusively ruled out.

3.5. Hardness measurement

The hardness of the LP-DED Ti-21S samples was evaluated by Vickers and nanoindentation, and the average values with standard deviations are reported in Fig. 9.

The measured microhardness values range from 332 to 388 HV, indicating that all processing conditions result in relatively high hardness levels, consistent with a fully β-stabilized titanium alloy. Based on the Fig. 9(a), L.E. = 50 J/mm exhibits the lowest average hardness, 332 ± 19.4 HV, whereas L.E. = 60 J/mm shows the highest value, 388 ± 15.4 HV. L.E. = 40 J/mm and L.E. = 47 J/mm present intermediate hardness levels of 357 ± 24.5 HV and 378 ± 12.6 HV, respectively. The relatively small scatter in the measurements for each condition demonstrates good local homogeneity within the tested regions and confirms the absence of large-scale microstructural or porosity variations, in agreement with the density and CT results.

The slight increase in hardness from L.E. = 47 J/mm to L.E. = 60 J/mm can be associated with differences in thermal history arising from the applied process parameters. Higher effective energy input and modified scanning conditions are expected to influence cooling rates, sub-grain structure, and the distribution of β-stabilizing elements (Mo, Nb), which in turn affect the solid-solution strengthening and dislocation density of the β matrix. Although the variations in hardness among the four parameter sets are modest, they suggest that fine tuning of LP-DED parameters can be used to subtly tailor the mechanical response of

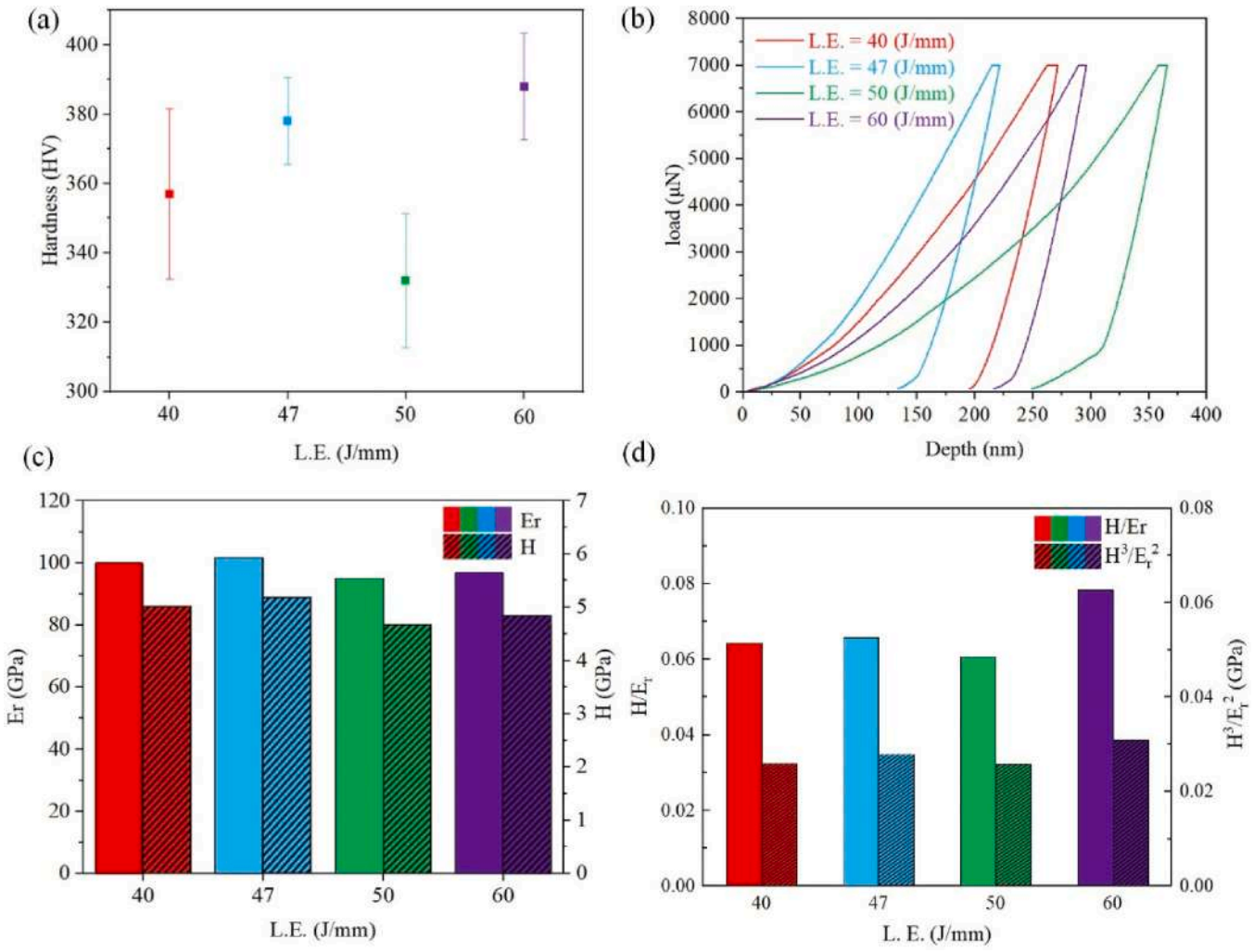


Fig. 9. (a) Micro-Vickers hardness (HV) results, (b) Nanoindentation curves, (c) hardness (H) and reduced elastic modulus (Er), (d) H/Er and H^3/Er^2 ratio for the four LP-DED Ti-21S samples.

Ti-21S without compromising densification. Previous studies investigating L-PBF of β-21S alloy have documented that both as-built and heat-treated specimens demonstrate a hardness value of approximately 380 ± 13 HV. This finding is consistent with the reported hardness of wrought β-21S subjected to solution treatment and aging (STA) at 871 °C for 30 min followed by air cooling, and subsequently aged at 538 °C for 8 h with air cooling, which exhibits a hardness of approximately 400 HV [10,47].

It was worth to be mentioned that a non-monotonic trend in hardness properties was observed as a function of L.E. with a distinct drop in microhardness at L.E. = 50 J/mm (Fig. 9a) compared to the lower energy levels. This behavior can be attributed to the complex thermal history inherent to the LP-DED process. At 40 and 47 J/mm, the rapid cooling rates likely promote a refined, supersaturated beta-matrix with high residual microstrain (as evidenced by the XRD data in Table 5), contributing to strain hardening. However, as the energy density increases to 50 J/mm, the increased heat input and slower cooling rates facilitate significant grain and crystallite coarsening (increasing from 27 nm to 32 nm), which according to the Hall-Petch relationship results in a reduction in hardness. The modest hardness recovery observed at 60 J/mm is attributed to thermal accumulation, minor interstitial solid-solution effects (O/N pickup) during prolonged high-temperature exposure, and matrix relaxation, remaining fully consistent with the single-phase bcc beta structure confirmed by XRD.

Nanoindentation tests were carried out to evaluate the local mechanical response of the LP-DED Ti-21S alloy at the submicrometric scale. Representative load–depth curves for the four processing conditions are shown in Fig. 9(b). All samples exhibit smooth loading and unloading segments without pop-in events, indicating the absence of brittle cracking or stress-induced phase transformations under the applied loads. For a comparable maximum load of ~6–7 mN, L.E. = 47 J/mm shows the lowest penetration depth, L.E. = 50 J/mm the highest, and L.E. = 40 J/mm and L.E. = 60 J/mm lie in between, qualitatively reflecting the relative hardness of the materials.

The hardness (H) and reduced elastic modulus (Er) values obtained by the Oliver–Pharr method [48] is summarized in Fig. 9(c). The reduced modulus falls within a narrow range of approximately 95–102 GPa, confirming that all parameter sets yield a β-Ti matrix with similar elastic stiffness. L.E. = 47 J/mm exhibits the highest Er and nano-hardness (around 5 GPa), followed by L.E. = 50 J/mm, while L.E. = 40 J/mm and L.E. = 60 J/mm show slightly lower hardness values (about 4–4.5 GPa). These trends are consistent with the penetration depths observed in the load–depth curves and with the Vickers microhardness measurements. It is well established that the microstructural characteristics of materials are directly correlated with their mechanical properties. Therefore, the observed reductions in hardness and reduced elastic modulus can be attributed to the microstructural features identified in this study.

Beyond evaluating hardness and elastic modulus, nanoindentation constitutes a valuable method for measuring multiple parameters that can be employed to predict the operational lifespan of a component. According to previous studies, the ratio of hardness to elastic modulus (H/Er) characterizes the resistance to elastic strain at failure, which is closely related to the wear behavior of materials [49,50]. Additionally, the ratio of hardness cubed to the square of the elastic modulus (H^3/Er^2) corresponds to the yield pressure, indicating the materials resistance to plastic deformation [51,52]. The values of H/Er and H^3/Er^2 are presented in Fig. 9(d). Higher values of these ratios are indicative of enhanced wear resistance and improved deformation resistance in materials [53].

Recent advancements in additively manufactured metastable beta-titanium alloys emphasize the critical balance between phase constitution, elastic modulus, and mechanical performance. As demonstrated in recent literature on L-PBF processed metastable beta-Ti systems (such as Ti-14Nb-6Zr-3Fe and derivative Sn/O-alloyed variants), controlling microstructural features like nanoscale omega-precipitates, dislocation cell networks, and grain morphology is essential for achieving an optimal combination of high strength, high elastic admissible strain, and a low elastic modulus. Similar to these observations, the LP-DED processed Ti-21S alloy preserves a fully retained beta-matrix with characteristic low elastic stiffness (95–102 GPa) and high microhardness, confirming that additive manufacturing routes can effectively tailor the mechanical and structural properties of advanced biomedical titanium alloys [54,55].

The good agreement between microhardness and nanoindentation data indicates that the observed differences are intrinsic to the material and not artefacts of a specific test method. Minor discrepancies in absolute hardness can be ascribed to the different probing volumes of the two techniques: Vickers microhardness averages over multiple grains and potential porosity, whereas nanoindentation probes individual β regions and is affected by indentation size effects. Overall, the results confirm that all LP-DED conditions produce a mechanically homogeneous β-Ti alloy with relatively low elastic modulus and promising characteristics for applications requiring a combination of high strength and reduced stiffness.

The observed variations in crystallite size and the reduction in lattice microstrain confirm that the intrinsic heat treatment (IHT) from successive laser passes induces a highly controlled in-situ annealing effect. Because the rapid solidification kinetics completely suppress alpha-phase precipitation, LP-DED yields a mechanically homogeneous matrix at the sub-micrometric scale, effectively preventing the localized stress concentrations typically found in dual-phase titanium alloys.

3.6. Electrochemical behaviour

3.6.1. electrochemical impedance spectroscopy (EIS)

While the macroscopic corrosion resistance of Ti-21S is well documented, the impact of AM on the nanoscale defect chemistry of its protective oxide layer remains unexplored. This section leverages the PDM to elucidate how the unique solid-solution matrix generated by LP-DED fundamentally alters the semiconducting properties of the passive film.

The corrosion resistance of the titanium alloys is attributed to the passive oxide film that develops on its surface [56–58]. To investigate the physicochemical changes occurring at the electrolyte/oxide/substrate interface and to evaluate the durability of the passive film, electrochemical behavior of the LP-DED Ti-21S alloy was characterized (see Fig. 10). The experimental data were modeled using an electrical equivalent circuit (EEC) consisting of a solution resistance (Rs) in series with a parallel combination of charge-transfer resistance (Rct) and a constant phase element (CPEdl), as shown in Fig. 11. This single-time-constant response indicates that the interfacial impedance is dominated by a stable passive film. The transition from an ideal capacitor to a CPE account for surface heterogeneities and structural defects within the oxide layer. High-quality fitting was confirmed by low chi-square ($chi^2 < 0.01$) values.

Fundamental to electrochemical theory, the impedance of a passive film is directly proportional to the radius of its Nyquist arc; thus, an expansion in the arc diameter signifies enhanced corrosion resistance. Across all tested conditions, the Nyquist plots maintained a consistent semi-circular morphology, with diameters increasing substantially as a function of immersion time. This trend suggests a progressive stabilization and thickening of the protective oxide layer. Notably, the Ti-21S alloy variants exhibited slightly larger arc radii than the Ti-6Al-4V reference, indicating a more robust interfacial barrier.

Based on data from Table 6 and among the LP-DED conditions, L.E. = 50 J/mm and L.E. = 47 J/mm display the highest charge-transfer resistances at long immersion times, with Rct values of 8.40×10^9 and 6.86×10^9 kΩ at 24 h, further increasing to 1.11×10^{10} and 1.06×10^{10} kΩ at 144 h, respectively. In comparison, L.E. = 40 J/mm and L.E. = 60 J/mm reach slightly lower but still very high Rct values (on the order of 6–7 × 10^9 kΩ after 144 h), comparable to those

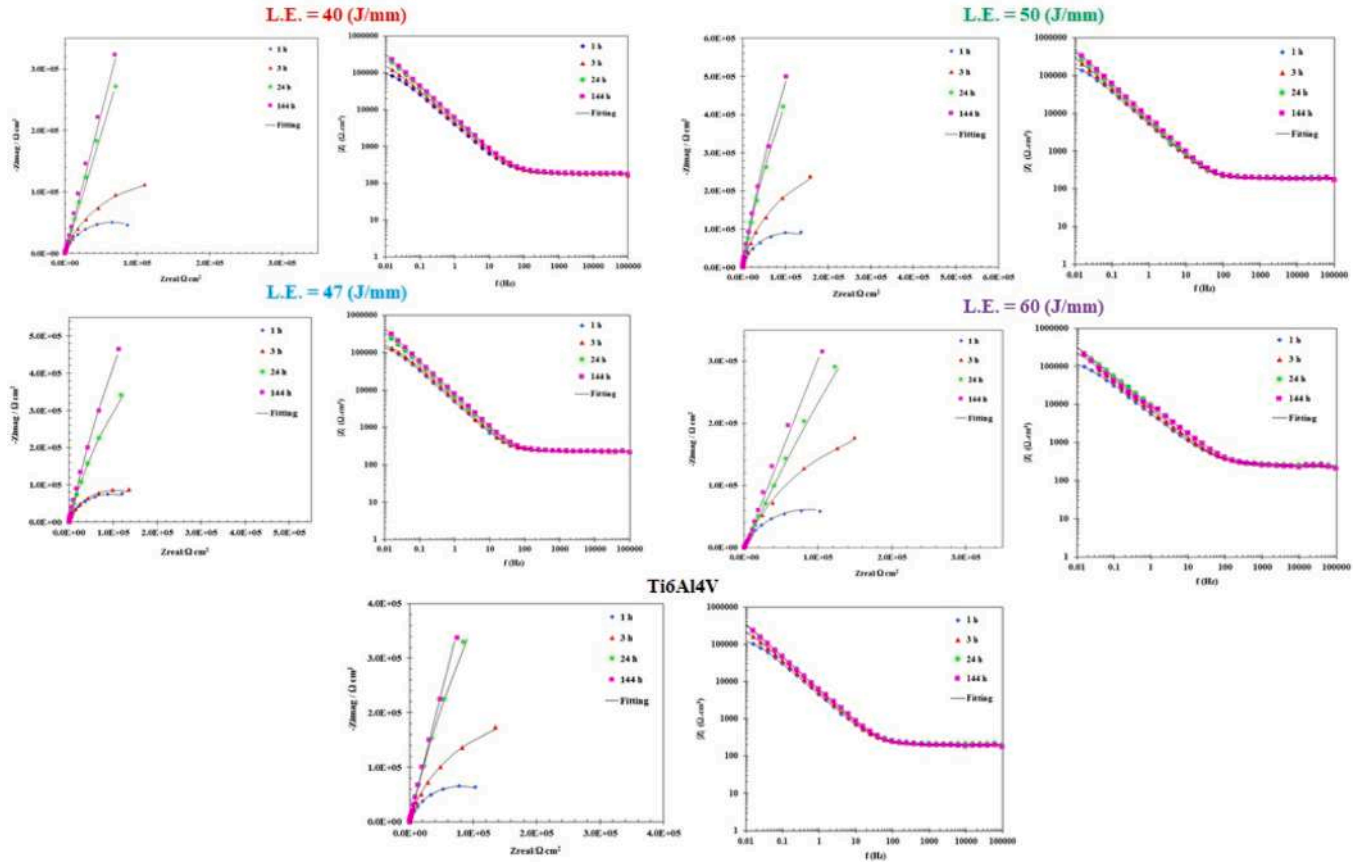


Fig. 10. Nyquist and Bode plots of samples at various time.

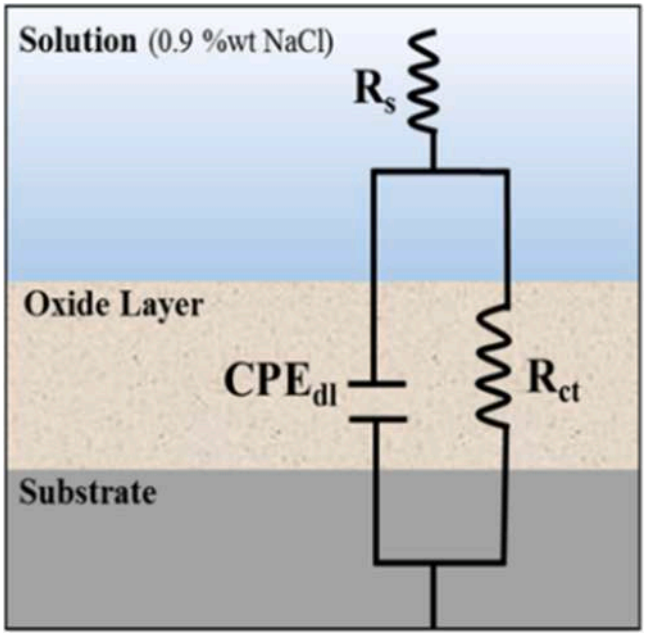


Fig. 11. Schematic of the electrical equivalent circuit of the specimens.

Table 6
Electrochemical data of the specimens in 0.9%wt NaCl solution for various durations, calculated from the circuit models.

L.E. (J/mm)	Time (h)	R_s (Ω)	R_{ct} (Ω)	Y_0 (μS)	N	χ^2
40	1	258.03	1.91×10^5	38	0.83	0.0031
	3	256.83	4.48×10^5	32.3	0.82	0.0036
	24	256.37	5.96×10^9	25.9	0.84	0.0027
	144	265.23	6.52×10^9	23.1	0.86	0.0032
47	1	330.14	2.72×10^5	29.4	0.86	0.0035
	3	332.29	3.06×10^5	25.5	0.86	0.0038
	24	334.6	6.86×10^9	20.7	0.87	0.0036
	144	325.45	1.06×10^{10}	17.2	0.88	0.003
50	1	274.97	3.15×10^5	26.6	0.88	0.0031
	3	278.71	9.79×10^5	23.5	0.88	0.0039
	24	285.1	8.40×10^9	20.2	0.91	0.0041
	144	266.72	1.11×10^{10}	17.1	0.91	0.0032
60	1	351.11	2.36×10^5	29.3	0.77	0.0017
	3	368.21	8.15×10^5	22.3	0.8	0.0042
	24	356.89	6.37×10^9	18	0.76	0.0038
	144	340.48	6.77×10^9	19.5	0.8	0.0039
Ti-6Al-4V	1	291.76	2.56×10^5	32.2	0.85	0.0035
	3	298.43	6.96×10^5	27.6	0.86	0.003
	24	302.12	6.16×10^9	22.4	0.88	0.003
	144	274.51	6.61×10^9	22.7	0.87	0.003

measured for the Ti-6Al-4V reference alloy (6.16×10^9 and 6.61×10^9 kΩ at 24 and 144 h, respectively). The consistently larger Rct values of L.E. = 47 J/mm and L.E. = 50 J/mm indicate that these LP-DED parameter sets promote the formation of a more resistive and stable passive film, resulting in superior corrosion resistance compared with both the other Ti-21S conditions and Ti-6Al-4V.

Comparative analysis reveals that the Ti-21S alloy exhibits superior passivity compared to the Ti-6Al-4V reference, primarily due to the synergistic effects of Mo and Nb alloying elements which facilitate the formation of a highly resistant Ti-Mo-Nb mixed oxide. While the solution resistance remained constant, the Rct values for Ti-21S increased by several orders of magnitude, reaching 10^9-10^{10} kΩ significantly outperforming the Ti-6Al-4V benchmark. This enhanced corrosion

resistance is attributed to the homogeneous beta-phase microstructure of the Ti-21S alloy, which lacks the more reactive alpha martensitic structures and complex alpha-beta phase boundaries found in Ti-6Al-4V.

Overall, the EIS results demonstrate that LP-DED Ti-21S develops an extremely protective passive layer in physiological NaCl solution, with corrosion resistance at least comparable to, and in some cases exceeding, that of Ti-6Al-4V. However, EIS provides a macroscopic average of surface properties, further insights into the semiconducting nature and

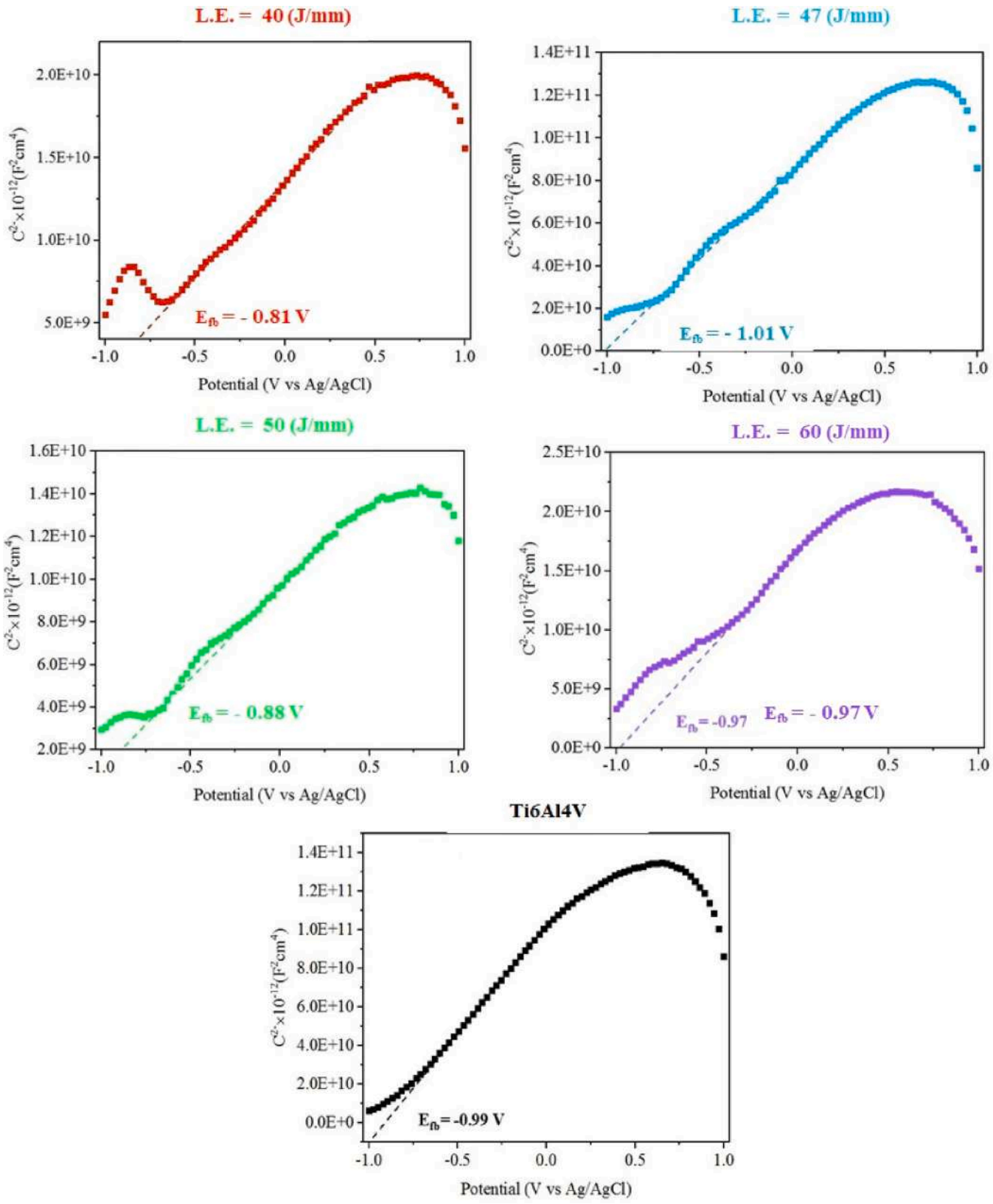


Fig. 12. Mott–Schottky (C-2 vs. E) plots for the passive films formed on LP-DED Ti-21S samples in 0.9 wt. NaCl solution.

electronic defects of these films will be addressed via Mott–Schottky analysis in the following section.

3.6.2. Mott–Schottky analysis

Further insight into the nature of the passive films was obtained from Mott–Schottky analysis, and the corresponding C^2–E plots for Ti-21S and Ti-6Al-4V are shown in Fig. 12. All specimens exhibit a positive slope in the linear region of the Mott–Schottky plots, indicating an n-type semiconducting behaviour of the passive layer, which is consistent with the predominance of TiO_2-based oxides doped by alloying elements such as Mo and Nb [59]. In n-type semiconducting oxides, the majority charge carriers are electrons, and the primary defects facilitating ionic transport (and therefore corrosion) are oxygen vacancies ($V_O^{\bullet\bullet}$) and titanium interstitials ($Ti_i^{\bullet\bullet\bullet\bullet}$). Moreover, the approximate linearity of the plots suggests that the passive films can be treated, to a first approximation, as uniform semiconductor layers within the investigated potential range.

The variation in slope among the samples qualitatively reflects differences in defect concentration within the oxide [59,60]. The variation in the slopes among the samples reflects differences in the apparent density of donor states within the passive films. According to the Mott–Schottky relationship, therefore, a steeper slope corresponds to a lower donor density, whereas a lower slope indicates a higher donor density. The Ti-21S conditions exhibiting the highest charge-transfer resistance in the EIS measurements (L.E. = 47 and 50 J/mm) were associated with a lower density of donor, indicating a lower population of electrically active donor defects and supporting the formation of a more compact and protective passive film [61].

Conversely, L.E. = 40 J/mm, L.E. = 60 J/mm present slightly steeper slopes, consistent with a higher defect density and the somewhat lower Rct values determined from the impedance spectra.

To elevate this observation into a robust physical model, donor density was calculated from the slope of the linear region of the M–S plots, using Eq. (3):

$$N_D = \frac{2}{\hat{\varepsilon}\varepsilon_0 e a} \tag{3}$$

where a is the slope of the $1/C_{sc}^2$–E plot, ε_0 stands for the vacuum permittivity (8.854×10^{-14} F.cm^{-1}) and, ε for the dielectric constant of the passive film (approximately 60 for the TiO_2 passive film [62]).

The donor density determined the apparent density of electrically active donor states within the space-charge region of the passive film. Although this parameter does not directly quantify a specific tpe of point defect, variations in the apparent donor density can be associated with changes in the population of donor-type defects, such as oxygen-vacancy-related states in passive films [63].

The calculated donor densities are approximately 1.63×10^{19} cm^{-3} for 21S (L.E. = 40 J/mm) and 3.62×10^{20} cm^{-3} for Ti-6Al-4V. These values align with those reported in the literature, where TiO_2-based passive films typically exhibit donor densities ranging from 10^{19} to 10^{20} cm^{-3} [64].

The comparatively lower apparent donor density obtained for Ti-21S (L.E. = 40 J/mm) indicates a lower population of electrically active donor states, which is consistent with a less defective and more protective passive film. Because oxygen vacancies are commonly regarded as donor-type defects in n-typeTiO_2-based passive films, the lower donor density may also indicate a reduced contribution from oxygen-vacancy-related donor states.

Conversely, Ti-6Al-4V displays a higher defect density, indicative of increased electronic conductivity and reduced passive film stability. Since oxygen vacancies are widely recognized as donor-type defects in n-type TiO_2-based passive films, an increased apparent donor density may be associated with a greater contribution of oxygen-vacancy-related donor states and enhanced electronic transport through the passive film [60,65].

Collectively, the EIS and Mott–Schottky analyses demonstrate that LP-DED Ti-21S develops a highly protective, n-type semiconducting passive film when exposed to a 0.9 wt% NaCl solution. Based on these findings, the schematic Fig. 13 illustrates two mechanisms that enhance the corrosion resistance of Ti-21S in comparison to Ti-6Al-4V: the influence of alloying elements on the passive layer, and the effects of the metal matrix phase and microstructure:

I. Influence of alloying elements on the passive layer

The oxides Nb_2O_5 and MoO_3 exhibit superior thermodynamic stability and protective qualities compared to TiO_2 modified by Al and V oxides [64,66]. In Ti-6Al-4V alloys, vanadium oxide often forms discrete agglomerates within the TiO_2 passive layer. These vanadium-rich zones compromise the passivity of the titanium alloy by creating conduction channels that facilitate electron and ion transport [5,67,68].

In the context of AM titanium alloys, the PDM characterizes oxygen vacancies as electron donor sites [69]. The inner passive film, also referred to as the barrier layer and located adjacent to the metal substrate, extends into the titanium matrix via a mechanism involving the condensation of cation and anion vacancies. This process is elucidated by the following chemical reactions (4−5) [70]:

$$Ti \rightarrow Ti_{Ti} + 2V_O^{\bullet\bullet} + 4e' \tag{4}$$

$$V_O^{\bullet\bullet} + O_2 + 4e' \rightarrow 2O_O \tag{5}$$

Here, Ti_{Ti} represents a titanium cation at a normal lattice site, while "•" and "′" denote positive and negative charges, respectively.

Oxygen vacancies ($V_O^{\bullet\bullet}$) are formed to preserve charge neutrality during the oxidation process of Ti^{3+} and Ti^{2+} to Ti^{4+}. The movement of these oxygen vacancies, titanium interstitials, and electrons collectively facilitates the overall development of the oxide layer. Concurrently, oxygen ions migrate in the opposite direction across the oxide layer via these vacancies [71,72].

The electric field and concentration gradient drive the migration of cation vacancies ($V_{Ti}^{4'}$) toward the interface between the metal and the barrier layer. At this interface, the accumulation of cation vacancies induces an increase in oxygen vacancies to maintain electroneutrality. The extent of these vacancy associations intensifies with the continued influx of cation vacancies [70,73]. Therefore, the system compensates for the depletion of oxygen vacancies through the generation of additional oxygen vacancies, a process driven by charge compensation mechanisms as described by Eq. (6) and associated with Schottky disorder.

$$4V_O^{\bullet\bullet} + 2V_{Ti}^{4'} \leftrightarrow Null' \tag{6}$$

From an alternative perspective, aggressive ions, such as chloride ions, permeate the hydroxide layer (the outer passive layer) adjacent to the solution and are subsequently adsorbed onto the oxide surface (Eq. (7)) [64,74]:

$$Cl_{aq}^- + * \leftrightarrow Cl^* + e' \tag{7}$$

The superscripts "-" and "*" represent a negative charge and an unoccupied site on the oxide surface, respectively. Chloride ions (Cl*) adsorbed onto the oxide layer are capable of migrating across its surface. A portion of these adsorbed chloride ions become immobilized by oxygen vacancies, resulting in the formation of $Cl_O^{\bullet}$ defects. (Eq. (8)).

$$Cl^* + V_O^{\bullet\bullet} + e' \leftrightarrow Cl_O^{\bullet} \tag{8}$$

Ultimately, the depletion of oxygen vacancies coupled with the formation of cation vacancies leads to significant aggregation and condensation of vacancies, culminating in the development of voids. These voids induce localized instability within the oxide layer, causing it to detach from the underlying metal substrate. The continued inward growth of the oxide subsequently results in the

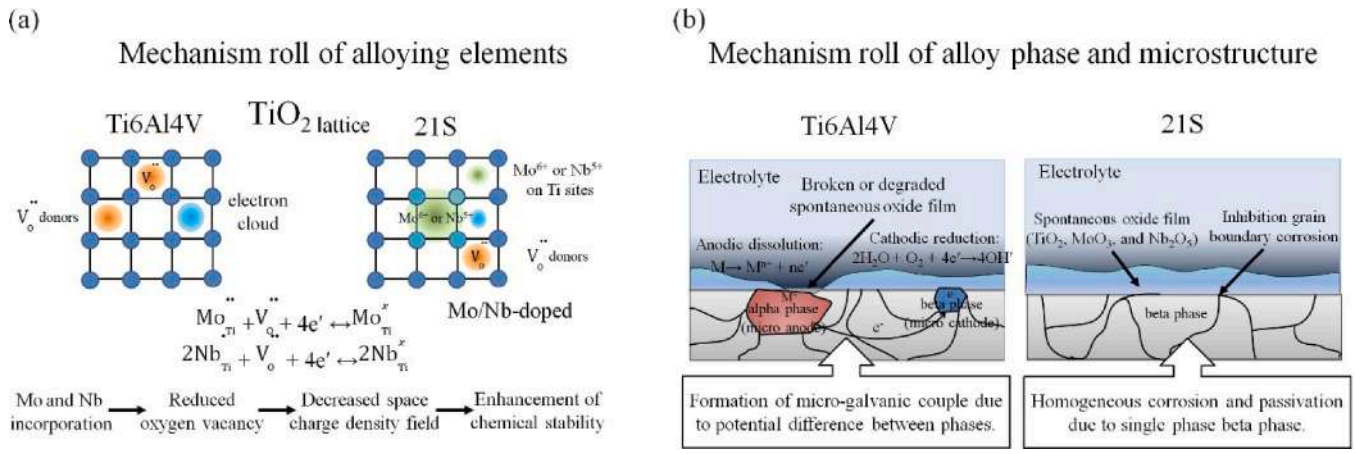


Fig. 13. Comprehensive analysis of passivation an corrosion mechanism in Ti-21S and Ti-6Al-4V, influence of (a) alloying elements, and (b) metal matrix phase and microstructure.

thinning and localized failure of the inner passive films at these void sites, a phenomenon attributed to the presence of tensile stresses (see Fig. 10c).

In the case of the 21S alloy, the reactions described in Eqs. (9,10), in which Mo_{Ti}^{x} and Nb_{Ti}^{x} were Mo and Nb site once it has been electronically compensated (becoming neutral relative to the lattice) suggest that the incorporation of high-valence elements such as Mo and Nb improves the chemical stability of the passive film, predominantly through alterations in its defect structure and diminishes the effective concentration of oxygen vacancy donors [71,75].

$$Mo_{Ti}^{\bullet\bullet} + V_O^{\bullet\bullet} + 4e' \leftrightarrow Mo_{Ti}^{x} \quad (9)$$

$$2Nb_{Ti}^{\bullet} + V_O^{\bullet\bullet} + 4e' \leftrightarrow 2Nb_{Ti}^{x} \quad (10)$$

where Mo_{Ti}^{x} and Nb_{Ti}^{x} were Mo and Nb site once it has been electronically compensated (becoming neutral relative to the lattice).

Based on the PDM framework and the measured reduction in donor densities, it is hypothesized that high-valence alloying elements such as Mo and Nb act as dopants within the passive layer. When incorporated into TiO_2, high-valence Mo and Nb species can modify the charge-compensation mechanism and defect chemistry of the oxide lattice. Their incorporation may therefore alter the population of oxygen-vacancy-related donor states and contribute to stabilization of the passive film.

Since these vacancies serve as the primary highways for ion transport through the oxide layer, as mentioned before, their reduction significantly decelerates the diffusion of corrosive species. This reduction in defect density leads to a more stoichiometric and compact oxide layer. Indeed, a denser electronic and physical structure makes the passive film significantly more resistant to the penetration of aggressive anions like Cl^- or F^-, effectively stifling the anodic dissolution process [74].

Furthermore, these alloying elements facilitate the transition from a simple oxide to a robust, multi-component passive layer consisting of a synergistic mixture of Ti-Nb-Mo oxide. This mixed-oxide configuration is characterized by higher thermodynamic stability and reduced solubility, particularly when exposed to aggressive acidic or fluoride-rich environments. Beyond structural stabilization, the presence of Molybdenum at the metal-oxide interface specifically suppresses anodic dissolution by inhibiting the hydration of metal ions. This chemical barrier makes it energetically difficult for the metal to transition into the electrolyte, providing a secondary layer of defense against localized breakdown and pitting [66,76].

All in all, by substituting Ti ions in passive layer with higher-valency Nb or Mo sites, the alloy effectively clogs the transport paths that oxygen and corrosive ions would otherwise use to eat away at the metal.

II. Phase and microstructure of matrix

Galvanic corrosion in titanium alloys is primarily driven by the electrochemical potential gradient established between distinct microstructural phases. In dual-phase alloys such as Ti-6Al-4V, the alpha phase (enriched with Al) functions as a micro-anode, while the beta phase (enriched with V) acts as a micro-cathode [5,77]. This configuration facilitates the preferential dissolution of the anodic alpha phase, particularly in components fabricated via LP-DED. The rapid cooling inherent in LP-DED produces a high-energy acicular alpha martensitic phase with small amount of beta phase is exceptionally susceptible to the breakdown of the protective oxide film, leading to localized pitting corrosion [78].

Conversely, single-phase beta-type alloys particularly 21S in this study, circumvent interphase galvanic coupling by maintaining a homogeneous microstructural chemistry. In these systems, electrochemical attack is typically restricted to high-energy grain boundaries where lattice mismatches occur [68]. However, as mentioned earlier, the integration of alloy elements like Mo and Nb promotes the formation of a highly stable, complex passivation layer (Ti-Nb-Mo oxide) that provides superior resistance to intergranular corrosion [64,79]. While these beta alloys exhibit excellent stability in biological fluids, their performance remains highly sensitive to the electrolyte chemistry; for instance, elevated fluoride concentrations can destabilize the passive film and reintroduce pitting vulnerabilities even in otherwise resistant single-phase systems.

Collectively, by effectively trapping high-valence Mo and Nb dopants in solid solution, the rapid solidification of LP-DED forces these elements to substitute Ti ion sites within the oxide lattice. The results show that the incorporation of Mo and Nb may contribute to stabilization of the electronic defect structure of the passive film.

Ultimately, this confirms that LP-DED can be strategically utilized not just for net-shape fabrication, but as a microstructural engineering tool to chemically stabilize the passive film and dictate the defect chemistry of advanced titanium alloys.

4. Conclusion

The present study established a mechanistic framework to understand how the rapid solidification kinetics of Laser Powder Directed Energy Deposition (LP-DED) govern the microstructural evolution, local mechanical properties, and surface passivation dynamics of the metastable beta-titanium alloy Ti-21S. Based on the experimental evaluations, the following fundamental conclusions are drawn:

1- By mapping the hydrodynamic stability of the LP-DED melt pool, it was demonstrated that an optimal energy threshold fundamentally stabilizes Marangoni convection. This thermodynamic stability successfully suppressed lack-of-fusion defects, enabling the fabrication of near-fully dense (99.7–99.9%) components with a chemically isotropic solid-solution matrix.

2- The extreme thermal gradients and rapid cooling rates inherent to LP-DED suppressed thermodynamically driven alpha-phase precipitation. This kinetic suppression yielded a fully retained beta-phase architecture. The resulting intrinsic heat treatments (IHT) induced submicrometric mechanical homogeneity, manifesting an optimal combination of elevated microhardness (332–388 HV) and low reduced elastic modulus (95–102 GPa) ideal for mitigating stress-shielding in biomedical applications.

3- Electrochemical evaluations integrated with the PDM revealed that the LP-DED thermal history effectively forces high-valence molybdenum and niobium solutes to act as n-type dopants within the oxide lattice. This microstructural engineering mechanism significantly reduced the concentration of oxygen vacancy donors, thermodynamically stabilizing the passive layer and yielding exceptional localized corrosion resistance that outperforms standard Ti-6Al-4V.

In summary, this research underscores that LP-DED can be strategically utilized not merely as a net-shape fabrication tool to bypass traditional manufacturing constraints, but as a robust microstructural engineering method to dictate the passivation dynamics and defect chemistry of advanced titanium alloys. To build upon these findings, future investigations should explore the impact of post-process heat treatments on the as-built AB microstructure, mechanical and corrosion properties. Indeed, advanced high-resolution characterization via transmission electron microscopy (TEM) and electron backscatter diffraction (EBSD) is necessary to completely rule out nanoscale precipitation and resolve local crystallographic textures completely suppressed. Similarly, explicit oxide stoichiometry via surface-sensitive spectroscopy (such as X-ray Photoelectron Spectroscopy (XPS)) remains to be conclusively established through targeted future surface analyses.

CRediT authorship contribution statement

Alireza Sohrabi: Writing – original draft, Methodology, Investigation, Formal analysis, Data curation. **Amir Behjat:** Writing – original draft, Validation, Software, Methodology, Investigation, Formal analysis, Conceptualization. **Federico Mazzucato:** Writing – review & editing, Validation, Methodology, Investigation, Formal analysis, Data curation. **Anna Valente:** Writing – review & editing, Resources, Investigation, Funding acquisition. **Arash Fattah-alhosseini:** Writing – review & editing, Supervision, Resources, Investigation, Funding acquisition, Formal analysis. **Razieh Chaharmahali:** Writing – review & editing, Validation, Methodology, Formal analysis, Data curation. **Luca Iuliano:** Writing – review & editing, Resources, Project administration, Investigation, Funding acquisition. **Abdollah Saboori:** Writing – review & editing, Validation, Supervision, Resources, Project administration, Investigation, Funding acquisition, Formal analysis, Conceptualization.

Declaration of Competing Interest

The authors declare that they have no known competing financial interests or personal relationships that could have appeared to influence the work reported in this paper.

References

[1] B. Dutta, F.H. (Sam) Froes, The Additive Manufacturing (AM) of titanium alloys, Met. Powder Rep. 72 (2017) 96–106, https://doi.org/10.1016/j.mprp.2016.12.062.

[2] R.P. Kolli, A. Devaraj, A Review of Metastable Beta Titanium Alloys, Metals 8 (2018) 506, https://doi.org/10.3390/met8070506.

[3] H.J. Rack, J.I. Qazi, Titanium alloys for biomedical applications, Mater. Sci. Eng. C. 26 (2006) 1269–1277, https://doi.org/10.1016/j.msec.2005.08.032.

[4] G. Lütjering, Influence of processing on microstructure and mechanical properties of (α+β) titanium alloys, Mater. Sci. Eng. A 243 (1998) 32–45, https://doi.org/10.1016/S0921-5093(97)00778-8.

[5] L. Zhou, T. Yuan, J. Tang, J. He, R. Li, Mechanical and corrosion behavior of titanium alloys additively manufactured by selective laser melting – A comparison between nearly β titanium, α titanium and α + β titanium, Opt. Laser Technol. 119 (2019) 105625, https://doi.org/10.1016/j.optlastec.2019.105625.

[6] L.-C. Zhang, L.-Y. Chen, S. Zhou, Z. Luo, Powder bed fusion manufacturing of beta-type titanium alloys for biomedical implant applications: A review, J. Alloy. Compd. 936 (2023) 168099, https://doi.org/10.1016/j.jallcom.2022.168099.

[7] 2003, C.LeyensM.PetersTitanium and Titanium AlloysWiley10.1002/3527602119.

[8] I. Weiss, S.L. Semiatin, Thermomechanical processing of beta titanium alloys—an overview, Mater. Sci. Eng. A 243 (1998) 46–65, https://doi.org/10.1016/S0921-5093(97)00783-1.

[9] F. Trevisan, F. Calignano, A. Aversa, G. Marchese, M. Lombardi, S. Biamino, D. Ugues, D. Manfredi, Additive manufacturing of titanium alloys in the biomedical field: processes, properties and applications, J. Appl. Biomater. Funct. Mater. 16 (2018) 57–67, https://doi.org/10.5301/jabfm.5000371.

[10] M.A. Macias-Sifuentes, C. Xu, O. Sanchez-Mata, S.Y. Kwon, S.E. Atabay, J. A. Muñiz-Lerma, M. Brochu, Microstructure and mechanical properties of β-21S Ti alloy fabricated through laser powder bed fusion, Prog. Addit. Manuf. 6 (2021) 417–430, https://doi.org/10.1007/s40964-021-00181-7.

[11] H. Ba, L. Dong, Z. Zhang, X. Lei, Effects of Trace Si Addition on the Microstructures and Tensile Properties of Ti-3Al-8V-6Cr-4Mo-4Zr Alloy, Metals 7 (2017) 286, https://doi.org/10.3390/met7080286.

[12] Y. Zhao, B. Li, Z. Zhu, Z. Nie, The high temperature deformation behavior and microstructure of TC21 titanium alloy, Mater. Sci. Eng. A 527 (2010) 5360–5367, https://doi.org/10.1016/j.msea.2010.05.076.

[13] S. Gain, D. Veeman, A review on advances and challenges in wire arc additive manufacturing: Process parameters, microstructural evolution and material performance across alloys, J. Alloy. Compd. 1029 (2025) 180735, https://doi.org/10.1016/j.jallcom.2025.180735.

[14] R. Banerjee, S. Nag, J. Stechschulte, H.L. Fraser, Strengthening mechanisms in Ti–Nb–Zr–Ta and Ti–Mo–Zr–Fe orthopaedic alloys, Biomaterials 25 (2004) 3413–3419, https://doi.org/10.1016/j.biomaterials.2003.10.041.

[15] A. Jam, M. Pellizzari, L. Emanuelli, G. Valsecchi, A. du Plessis, M. Benedetti, Influence of heat treatment on the mechanical performance of Ti21S octet truss lattice structure fabricated by laser powder bed fusion, Prog. Addit. Manuf. 9 (2024) 947–957, https://doi.org/10.1007/s40964-023-00494-9.

[16] S.L. Semiatin, N. Frey, S.M. El-Soudani, J.D. Bryant, Flow softening and microstructure evolution during hot working of wrought near-gamma titanium aluminides, Metall. Trans. A 23 (1992) 1719–1735, https://doi.org/10.1007/BF02804366.

[17] Y.G. Zhou, W.D. Zeng, H.Q. Yu, An investigation of a new near-beta forging process for titanium alloys and its application in aviation components, Mater. Sci. Eng. A 393 (2005) 204–212, https://doi.org/10.1016/j.msea.2004.10.016.

[18] T. Childerhouse, M. Jackson, Near Net Shape Manufacture of Titanium Alloy Components from Powder and Wire: A Review of State-of-the-Art Process Routes, Met. (Basel) 9 (2019) 689, https://doi.org/10.3390/met9060689.

[19] B. Jin, Q. Wang, L. Zhao, A. Pan, X. Ding, W. Gao, Y. Song, X. Zhang, A Review of Additive Manufacturing Techniques and Post-Processing for High-Temperature Titanium Alloys, Met. (Basel) 13 (2023) 1327, https://doi.org/10.3390/met13081327.

[20] A. Behjat, S. Sanaei, M.H. Mosallanejad, M. Atapour, A. Saboori, Electrochemical Behavior of Electron Beam Powder Bed Fused Ti536 Alloy under Simulated Inflammatory Conditions, Acta Metall. Sin. (Engl. Lett. 38 (2025) 969–980, https://doi.org/10.1007/s40195-025-01846-w.

[21] H.Y. Ma, J.C. Wang, P. Qin, Y.J. Liu, L.Y. Chen, L.Q. Wang, L.C. Zhang, Advances in additively manufactured titanium alloys by powder bed fusion and directed energy deposition: Microstructure, defects, and mechanical behavior, J. Mater. Sci. Technol. 183 (2024) 32–62, https://doi.org/10.1016/j.jmst.2023.11.003.

[22] M. Bakhshi, F. Ranjkesh, A. Behjat, E. Atzeni, A. Saboori, Engineering titanium alloys for additive manufacturing: Feedstock design, solidification control, and functional properties, J. Alloy. Compd. 1080 (2026) 190707, https://doi.org/10.1016/j.jallcom.2026.190707.

[23] G. Piscopo, E. Atzeni, A. Saboori, A. Salmi, An Overview of the Process Mechanisms in the Laser Powder Directed Energy Deposition, Appl. Sci. 13 (2022) 117, https://doi.org/10.3390/app13010117.

[24] T. Zhang, C.-T. Liu, Design of titanium alloys by additive manufacturing: A critical review, Adv. Powder Mater. 1 (2022) 100014, https://doi.org/10.1016/j.apmate.2021.11.001.

[25] A.W. Prabhu, T. Vincent, A. Chaudhary, W. Zhang, S.S. Babu, Effect of microstructure and defects on fatigue behaviour of directed energy deposited Ti–6Al–4V, Sci. Technol. Weld. Join. 20 (2015) 659–669, https://doi.org/10.1179/1362171815Y.0000000050.

[26] A. Behjat, Y. Aghayar, A. Shahriari, M. Mohammadi, L. Iuliano, A. Saboori, Processing–structure–property relationships in Ti–6Al–2Sn–4Zr–2Mo alloy processed via different direct additive manufacturing technologies, J. Alloy. Compd. 1075 (2026) 189242, https://doi.org/10.1016/j.jallcom.2026.189242.

[27] A. Jam, A. du Plessis, C. Lora, S. Raghavendra, M. Pellizzari, M. Benedetti, Manufacturability of lattice structures fabricated by laser powder bed fusion: A novel biomedical application of the beta Ti-21S alloy, Addit. Manuf. 50 (2022) 102556, https://doi.org/10.1016/j.addma.2021.102556.

[28] A. Saboori, D. Gallo, S. Biamino, P. Fino, M. Lombardi, An Overview of Additive Manufacturing of Titanium Components by Directed Energy Deposition: Microstructure and Mechanical Properties, Appl. Sci. 7 (2017) 883, https://doi.org/10.3390/app7090883.
[29] N.A. Gosse, I.W. Donaldson, D.P. Bishop, Directed energy deposition processing of titanium alloys Ti-6242 and Beta 21S, Can. Metall. Q. 64 (2025) 1663–1683, https://doi.org/10.1080/00084433.2024.2367189.
[30] G. Wang, X. Chen, Z. Xu, F. Feng, J. Zhang, X. Zhang, P. Feng, Advanced Precision Cutting Titanium Alloy Methods: A Critical Review Considering Cost, Efficiency, and Quality, Technologies 13 (2025) 172, https://doi.org/10.3390/technologies13050172.
[31] J.C. Williams, R.R. Boyer, Opportunities and Issues in the Application of Titanium Alloys for Aerospace Components, Met. (Basel) 10 (2020) 705, https://doi.org/10.3390/met10060705.
[32] A. Saboori, S. Tusacciu, M. Busatto, M. Lai, S. Biamino, P. Fino, M. Lombardi, Production of Single Tracks of Ti-6Al-4V by Directed Energy Deposition to Determine the Layer Thickness for Multilayer Deposition, J. Vis. Exp. (2018), https://doi.org/10.3791/56966.
[33] L. Haferkamp, L. Haudenschild, A. Spierings, K. Wegener, K. Riener, S. Ziegelmeier, G.J. Leichtfried, The Influence of Particle Shape, Powder Flowability, and Powder Layer Density on Part Density in Laser Powder Bed Fusion, Met. (Basel) 11 (2021) 418, https://doi.org/10.3390/met11030418.
[34] S. Zhang, K. Guo, Y. Qing, C. Liu, Research Progress on the Preparation Technology of Spherical Alloy Powders for Laser Additive Manufacturing, Mater. (Basel) 18 (2025) 3385, https://doi.org/10.3390/ma18143385.
[35] S.E. Brika, M. Letenneur, C.A. Dion, V. Brailovski, Influence of particle morphology and size distribution on the powder flowability and laser powder bed fusion manufacturability of Ti-6Al-4V alloy, Addit. Manuf. 31 (2020) 100929, https://doi.org/10.1016/j.addma.2019.100929.
[36] A. Dareh Baghi, S. Nafisi, H. Ebendorff-Heidepriem, R. Ghomashchi, Microstructural Development of Ti-6Al-4V Alloy via Powder Metallurgy and Laser Powder Bed Fusion, Met. (Basel) 12 (2022) 1462, https://doi.org/10.3390/met12091462.
[37] W.H. Kan, L.N.S. Chiu, C.V.S. Lim, Y. Zhu, Y. Tian, D. Jiang, A. Huang, A critical review on the effects of process-induced porosity on the mechanical properties of alloys fabricated by laser powder bed fusion, J. Mater. Sci. 57 (2022) 9818–9865, https://doi.org/10.1007/s10853-022-06990-7.
[38] C. Kledwig, H. Perfahl, M. Reisacher, F. Brückner, J. Bliedtner, C. Leyens, Analysis of Melt Pool Characteristics and Process Parameters Using a Coaxial Monitoring System during Directed Energy Deposition in Additive Manufacturing, Mater. (Basel) 12 (2019) 308, https://doi.org/10.3390/ma12020308.
[39] M. Maleki, A.R. Eivani, M. Tayebi, J. Sherafati, H.R. Jafarian, Correlations in LPBF-fabricated Ti6Al4V: Influence of laser power and scanning speed on microstructure and mechanical performance, Results Eng. 29 (2026) 109122, https://doi.org/10.1016/j.rineng.2026.109122.
[40] P. Akbari, F. Ogoke, N.-Y. Kao, K. Meidani, C.-Y. Yeh, W. Lee, A. Barati Farimani, MeltpoolNet: Melt pool characteristic prediction in Metal Additive Manufacturing using machine learning, Addit. Manuf. 55 (2022) 102817, https://doi.org/10.1016/j.addma.2022.102817.
[41] H.-H. König, N.H. Pettersson, A. Durga, S. Van Petegem, D. Grolimund, A. C. Chuang, Q. Guo, L. Chen, C. Oikonomou, F. Zhang, G. Lindwall, Solidification modes during additive manufacturing of steel revealed by high-speed X-ray diffraction, Acta Mater. 246 (2023) 118713, https://doi.org/10.1016/j.actamat.2023.118713.
[42] A. Behjat, M. Shamanian, F. Sadeghi, M.H. Mosallanejad, A. Saboori, Process-Driven Structural and Property Evolution in Laser Powder Bed Fusion of a Newly Developed AISI 316L Stainless Steel, Mater. (Basel) 18 (2025) 3343, https://doi.org/10.3390/ma18143343.
[43] S. Chandra, J. Radhakrishnan, S. Huang, S. Wei, U. Ramamurty, Solidification in metal additive manufacturing: challenges, solutions, and opportunities, Prog. Mater. Sci. 148 (2025) 101361, https://doi.org/10.1016/j.pmatsci.2024.101361.
[44] A. Takase, T. Ishimoto, R. Suganuma, T. Nakano, Surface residual stress and phase stability in unstable β-type Ti–15Mo–5Zr–3Al alloy manufactured by laser and electron beam powder bed fusion technologies, Addit. Manuf. 47 (2021) 102257, https://doi.org/10.1016/j.addma.2021.102257.
[45] S.-H. Sun, K. Hagihara, T. Ishimoto, R. Suganuma, Y.-F. Xue, T. Nakano, Comparison of microstructure, crystallographic texture, and mechanical properties in Ti–15Mo–5Zr–3Al alloys fabricated via electron and laser beam powder bed fusion technologies, Addit. Manuf. 47 (2021) 102329, https://doi.org/10.1016/j.addma.2021.102329.
[46] Y. Li, J. Yi, H. Zhang, C. Liu, J. Gu, S. Ni, X. Liu, B. Guo, Z. Wu, I. Baker, M. Song, Unleashing superior strength and ductility in additively manufactured β-titanium alloys through spinodal decomposition, Adv. Powder Mater. 5 (2026), https://doi.org/10.1016/j.apmate.2026.100428.
[47] G.A. Young, J.R. Scully, Effects of hydrogen on the mechanical properties of a TiMoNbAl alloy, Scr. Metall. Mater. 28 (1993) 507–512, https://doi.org/10.1016/0956-716X(93)90091-6.
[48] W.C. Oliver, G.M. Pharr, An improved technique for determining hardness and elastic modulus using load and displacement sensing indentation experiments, J. Mater. Res. 7 (1992) 1564–1583, https://doi.org/10.1557/jmr.1992.1564.
[49] S. Demirci, T. Dikici, R. Dalmis, Nanoindentation and Corrosion Behavior of Additively Manufactured Ti-6Al-4V Alloy for Biomaterial Applications, J. Mater. Eng. Perform. 33 (2024) 2133–2145, https://doi.org/10.1007/s11665-023-08139-2.
[50] A. Hynowska, E. Pellicer, J. Fornell, S. González, N. van Steenberge, S. Suriñach, A. Gebert, M. Calin, J. Eckert, M.D. Baró, J. Sort, Nanostructured β-phase Ti–31.0Fe–9.0Sn and sub-μm structured Ti–39.3Nb–13.3Zr–10.7Ta alloys for biomedical applications: Microstructure benefits on the mechanical and corrosion performances, Mater. Sci. Eng. C. 32 (2012) 2418–2425, https://doi.org/10.1016/j.msec.2012.07.016.
[51] K. Vutova, V. Vassileva, V. Stefanova, M. Naplatanova, in: Z. Peng, J.-Y. Hwang, J. P. Downey, D. Gregurek, B. Zhao, O. Yücel, E. Keskinkilic, T. Jiang, J.F. White, M. M. Mahmoud (Eds.), Influence of Process Parameters on the Metal Quality at Electron Beam Melting of Molybdenum BT - 11th International Symposium on High-Temperature Metallurgical Processing, Springer International Publishing, Cham, 2020, pp. 941–951.
[52] Y.W. Bao, W. Wang, Y.C. Zhou, Investigation of the relationship between elastic modulus and hardness based on depth-sensing indentation measurements, Acta Mater. 52 (2004) 5397–5404, https://doi.org/10.1016/j.actamat.2004.08.002.
[53] H. Attar, S. Ehtemam-Haghighi, D. Kent, I.V. Okulov, H. Wendrock, M. Bönisch, A. S. Volegov, M. Calin, J. Eckert, M.S. Dargusch, Nanoindentation and wear properties of Ti and Ti-TiB composite materials produced by selective laser melting, Mater. Sci. Eng. A 688 (2017) 20–26, https://doi.org/10.1016/j.msea.2017.01.096.
[54] Y. Li, H. Wu, F. Ding, R. Hao, M. Lei, X. Li, M. Yan, J. Cao, Y. Li, Exceptional strength–ductility–modulus combination in additively manufactured metastable β titanium alloy via synergistic tuning of strengthening mechanisms, Mater. Sci. Eng. A 959 (2026), https://doi.org/10.1016/j.msea.2026.150057.
[55] Y. Li, L. Wang, H. Wu, F. Ding, M. Lei, J. Yang, J.P. Oliveira, M. Yan, W. Guo, Y. Li, High strength, low modulus, and ductile metastable beta Ti-Nb-Zr-Fe alloys by laser powder bed fusion in-situ alloying, J. Mater. Sci. Technol. 241 (2026) 270–283, https://doi.org/10.1016/j.jmst.2025.02.083.
[56] A. Li, Q. Wang, R. Chen, X. Ding, Y. Su, H. Fu, Application of alloying for enhancing the corrosion resistance of titanium alloys: A review, Mater. Today Commun. 42 (2025) 111111, https://doi.org/10.1016/j.mtcomm.2024.111111.
[57] A. Behjat, S. Sanaei, M.H. Mosallanejad, M. Atapour, M. Sheikholeslam, A. Saboori, L. Iuliano, A novel titanium alloy for load-bearing biomedical implants: Evaluating the antibacterial and biocompatibility of Ti536 produced via electron beam powder bed fusion additive manufacturing process, Biomater. Adv. 163 (2024) 213928, https://doi.org/10.1016/j.bioadv.2024.213928.
[58] T. Hanawa, Biocompatibility of titanium from the viewpoint of its surface, Sci. Technol. Adv. Mater. 23 (2022) 457–472, https://doi.org/10.1080/14686996.2022.2106156.
[59] A. Fattah-alhosseini, F. Soltani, F. Shirsalimi, B. Ezadi, N. Attarzadeh, The semiconducting properties of passive films formed on AISI 316 L and AISI 321 stainless steels: A test of the point defect model (PDM), Corros. Sci. 53 (2011) 3186–3192, https://doi.org/10.1016/j.corsci.2011.05.063.
[60] A. behjat, A. Saboori, M. Galati, L. Iuliano, The electrochemical behaviour of Ti-48Al-2Cr-2Nb produced by electron beam powder bed fusion process, Intermetallics 175 (2024) 108472, https://doi.org/10.1016/j.intermet.2024.108472.
[61] D.-I. Seo, J.-B. Lee, Localized Corrosion Resistance on Additively Manufactured Ti Alloys by Means of Electrochemical Critical Localized Corrosion Potential in Biomedical Solution Environments, Mater. (Basel) 14 (2021) 7481, https://doi.org/10.3390/ma14237481.
[62] X. Gai, Y. Bai, J. Li, S. Li, W. Hou, Y. Hao, X. Zhang, R. Yang, R.D.K. Misra, Electrochemical behaviour of passive film formed on the surface of Ti-6Al-4V alloys fabricated by electron beam melting, Corros. Sci. 145 (2018) 80–89, https://doi.org/10.1016/j.corsci.2018.09.010.
[63] Q. Zhang, Y. Tian, D. Liu, H. Zhang, J. Chen, Z. Zhao, Q. Feng, W. Gao, Q. Wang, H. Yu, D. Sun, Passive Film Degradation and Microbiologically Influenced Corrosion Mechanism of β Titanium Alloy Induced by Pseudomonas aeruginosa Biofilms, Met. (Basel) 16 (2026) 840, https://doi.org/10.3390/met16080840.
[64] D.-I. Seo, J.-B. Lee, Localized corrosion and repassivation behaviors of additively manufactured titanium alloys in simulated biomedical solutions, Npj Mater. Degrad. 7 (2023) 44, https://doi.org/10.1038/s41529-023-00363-4.
[65] Z. Jiang, X. Dai, T. Norby, H. Middleton, Investigation of pitting resistance of titanium based on a modified point defect model, Corros. Sci. 53 (2011) 815–821, https://doi.org/10.1016/j.corsci.2010.11.015.
[66] A. Akman, Y. Douest, L.A. Alberta, K. Perrin, A.-M. Trunfio Sfarghiu, N. Courtois, B. Ter-Ovanessian, S. Pilz, M. Zimmermann, M. Calin, A. Gebert, Tribocorrosion behaviour of additively manufactured β-type Ti–Nb alloy for implant applications, J. Mater. Res. Technol. 31 (2024) 1419–1429, https://doi.org/10.1016/j.jmrt.2024.06.172.
[67] V. Dehnavi, J.D. Henderson, C. Dharmendra, B.S. Amirkhiz, D.W. Shoesmith, J. J. Noël, M. Mohammadi, Corrosion Behaviour of Electron Beam Melted Ti6Al4V: Effects of Microstructural Variation, J. Electrochem. Soc. 167 (2020) 131505, https://doi.org/10.1149/1945-7111/abb9d1.
[68] U. Nichul, V. Kumar, V. Hiwarkar, Electrochemical performance of heat-treated beta titanium alloy in artificial saliva: Key role of grain size, Mater. Today Commun. 37 (2023) 106981, https://doi.org/10.1016/j.mtcomm.2023.106981.
[69] D.D. Macdonald, The Point Defect Model for the Passive State, J. Electrochem. Soc. 139 (1992) 3434–3449, https://doi.org/10.1149/1.2069096.
[70] Z. Jiang, X. Dai, T. Norby, H. Middleton, Investigation of pitting resistance of titanium based on a modified point defect model, Corros. Sci. 53 (2011) 815–821, https://doi.org/10.1016/j.corsci.2010.11.015.
[71] M. Metikoš-Huković, A. Kwokal, J. Piljac, The influence of niobium and vanadium on passivity of titanium-based implants in physiological solution, Biomaterials 24 (2003) 3765–3775, https://doi.org/10.1016/S0142-9612(03)00252-7.
[72] Y.-W. Cui, L.-Y. Chen, Y.-H. Chu, L. Zhang, R. Li, S. Lu, L. Wang, L.-C. Zhang, Metastable pitting corrosion behavior and characteristics of passive film of laser powder bed fusion produced Ti–6Al–4V in NaCl solutions with different

concentrations, Corros. Sci. 215 (2023) 111017, https://doi.org/10.1016/j.corsci.2023.111017.
[73] L.-Y. Chen, H.-Y. Zhang, C. Zheng, H.-Y. Yang, P. Qin, C. Zhao, S. Lu, S.-X. Liang, L. Chai, L.-C. Zhang, Corrosion behavior and characteristics of passive films of laser powder bed fusion produced Ti–6Al–4V in dynamic Hank's solution, Mater. Des. 208 (2021) 109907, https://doi.org/10.1016/j.matdes.2021.109907.
[74] H.-H. Huang, Effects of fluoride concentration and elastic tensile strain on the corrosion resistance of commercially pure titanium, Biomaterials 23 (2002) 59–63, https://doi.org/10.1016/S0142-9612(01)00079-5.
[75] M. Seo, G. Hultquist, C. Leygraf, N. Sato, The influence of minor alloying elements (Nb, Ti and Cu) on the corrosion resistivity of ferritic stainless steel in sulfuric acid solution, Corros. Sci. 26 (1986) 949–960, https://doi.org/10.1016/0010-938X(86)90085-5.
[76] T. Qin, X. Lin, J. Yu, M. Wang, P. Guo, J. Li, Y. Zhang, J. Liu, S. Zhang, W. Huang, Performance of different microstructure on electrochemical behaviors of laser solid formed Ti–6Al–4V alloy in NaCl solution, Corros. Sci. 185 (2021) 109392, https://doi.org/10.1016/j.corsci.2021.109392.
[77] X. Zhou, D. Xu, S. Geng, Y. Fan, C. Yang, Q. Wang, F. Wang, Microstructural evolution and corrosion behavior of Ti–6Al–4V alloy fabricated by laser metal deposition for dental applications, J. Mater. Res. Technol. 14 (2021) 1459–1472, https://doi.org/10.1016/j.jmrt.2021.07.006.
[78] M.K. Zadeh, M. Yeganeh, M.T. Shoushtari, H. Ramezanalizadeh, F. Seidi, Microstructure, corrosion behavior, and biocompatibility of Ti-6Al-4 V alloy fabricated by LPBF and EBM techniques, Mater. Today Commun. 31 (2022) 103502, https://doi.org/10.1016/j.mtcomm.2022.103502.
[79] J. Li, L. Zhu, C. Feng, K. Zhang, C. Huo, Review on Alloying Elements effects for Surface Film Structure and Corrosion Resistance of Titanium Alloys, J. Phys. Conf. Ser. 3129 (2025) 012046, https://doi.org/10.1088/1742-6596/3129/1/012046.